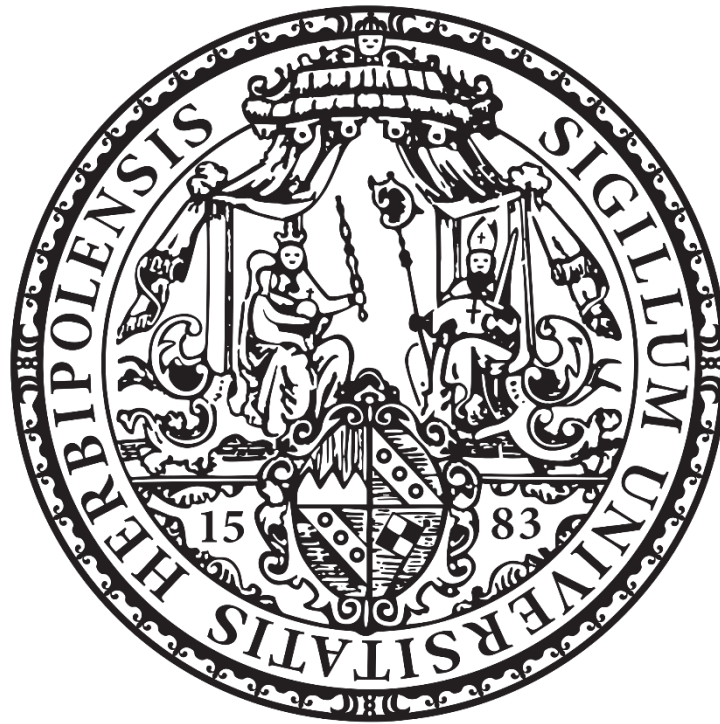


Julius-Maximilians-Universität Würzburg
Faculty of Physics and Astronomy



Radio Observations of the γ -flaring Blazar PKS 1451-375

A thesis submitted in fulfilment of the requirements
for the degree of Bachelor of Science

Author: Luis Wachter

Supervisor: Prof. Dr. Matthias Kadler

Date of Submission: March 29, 2018

Zusammenfassung

Aktive Galaxienkerne (AGN) sind kompakte Regionen im Zentrum ihrer Galaxie in denen Akkretion von Masse auf ein supermassives schwarzes Loch große Mengen an Energie freisetzt. Einige dieser Quellen zeigen Plasma Jets in denen Teilchen auf hoch-relativistische Geschwindigkeiten senkrecht zu der Akkretionsscheibe um das schwarze Loch beschleunigt werden. Das vereinheitlichende Modell von AGN schlägt vor, dass die Beobachtung eines solchen Objekts bei kleinen Sichtwinkeln einen Blazar zeigt, die in leuchtschwache BL Lac Objekte und leuchtstarke FSRQ unterteilt werden. Die Beobachtung des gleichen Objekts bei größeren Sichtwinkeln relativ zum Jet zeigt eine Radiogalaxie, die in leuchtschwache FR 1 und leuchtstarke FR 2 Galaxien unterteilt werden. In diesem Modell, FSRQ sind die gedrehten und gebeamteten Gegenstücke zu FR 2 Galaxien und BL Lacs die Gegenstücke zu FR 1 Galaxien. FR 2 Galaxien zeigen einen hellen Kern zusammen mit einem häufig einseitigen Jet und zwei hellen Hotspots in entgegengesetzten Richtungen zum Kern.

PKS 1451-375 ist ein Beispiel eines AGN der ursprünglich klassifiziert wurde als Quasar oder möglicherweise FSRQ. Vorherige hochauflösende Beobachtungen zeigt ein kompaktes Objekt mit hellem Kern und einem Jet in südwestliche Richtung. Eine Observation mit dem VLA bei 5 GHz zeigte ebenfalls einen Jet in südwestlicher Richtung, eine andere ebenfalls mit dem VLA durchgeführte Beobachtung bei 1.5 GHz zeigte einen hellen Kern mit zwei Hotspots.

In dieser Arbeit wird eine hochauflösende Beobachtung von PKS 1451-375 mit TANAMI bei 8.4 GHz sowie eine Beobachtung mit dem VLA bei 4.8 GHz analysiert. TANAMI ist ein Langbasisinterferometrie Programm das Antennen auf der Südhalbkugel nutzt, was es zum einzigen VLBI Programm macht, das südlicher als -30° beobachten kann. Die Beobachtung mit TANAMI wurde auf Grund eines erhöhten Flusses, beobachten vom Fermi Satelliten, durchgeführt. Die Fermi-Lichtkurve zeigt keinen ausgeprägten Fluss, mit Ausnahme eines Ausbruchs im Oktober 2012. Die TANAMI Beobachtung zeigt einen hellen Kern mit einem 5 mas langem Jet in südwestlicher Richtung während die VLA Beobachtung einen hellen Kern mit einem einseitigen Jet und zwei Hotspots in entgegengesetzten Richtungen vom Kern zeigt, was einer typischen FR 2 Morphologie entspricht.

Eine Komponentenanalyse zeigt, dass der Jet nahezu konisch ist und die Geometrie über beide Beobachtungen hinweg konstant ist mit einem Potenzgesetz von $l = 0.960 \pm 0.033$ zwischen der Größe der Komponenten und der Entfernung vom Kern. Der Gradient der Helligkeitstemperatur zeigt ebenfalls ein Potenzgesetz mit einem Exponenten von $s_{TANAMI} = -3.46 \pm 0.14$ für die TANAMI Beobachtung und $s_{VLA} = -1.34 \pm 0.50$ für die VLA Beobachtung, wobei $s = l + n + b(1 - \alpha)$ mit den Potenzgesetzexponenten l für die Jet Geometrie, n für die Teilchendichte, b für das Magnetfeld und α der Spektralindex. Dies lässt vermuten, dass eine Änderung im Jet stattfindet, die entweder das Magnetfeld, die Teilchendichte oder den Spektralindex ändert, mit der Annahme, dass alle drei von Potenzgesetzen beschrieben werden. Der Kern der TANAMI Beobachtung zeigt mit $T_b = 2.1 \cdot 10^{11}$ K eine Helligkeitstemperatur über dem Equipartitionslimit.

Der Sichtwinkel wird durch das Verhältnis der Flussdichte des Jets zum Gegenjet in der TANAMI Beobachtung auf $\phi < 22.5^\circ$ eingeschränkt und mit einer anderen Methode die den scheinbaren Öffnungswinkel des Jets mit ähnlichen Quellen vergleicht auf $\phi_{SW} > 52.5^\circ$ und $\phi_{NE} > 32.1^\circ$ für die beiden Hotspots. Auch wenn beide Resultate nicht konsistent sind, was an zu klein veranschlagte Hotspots liegen könnte, scheint PKS 1451-375 dennoch nicht so kleine Sichtwinkel wie Blazare zu zeigen.

Abstract

Active galactic nuclei (AGN) are compact regions in the center of their host galaxy, where accretion of mass on a supermassive black hole can release a substantial amount of energy. Some of these sources show plasma jets where particles get accelerated to highly relativistic speeds perpendicular to the accretion disk around the black hole. The unification model of AGN suggests that if such an object is observed at a small inclination angle it is seen as blazars that are divided into low-power BL Lac objects and high-power FSRQ and the same object observed at high inclination angles relative to the jet is seen as a radio galaxy that are divided into low power FR 1 and high power FR 2 galaxies. In this model, FSRQ are the rotated and beamed counterparts to FR 2 galaxies and Bl Lacs the rotated counterpart to FR 1 galaxies. FR 2 galaxies show a bright core with an often one-sided jet and two bright hotspots in opposite directions from the core.

PKS 1451-375 is an AGN that was initially classified as a quasar or a possible FSRQ. High-resolution images revealed a compact object with a bright core and a jet pointing in a south-western direction. One observation obtained with the VLA at 5 GHz showed as well a jet in a south-western direction and another observation with the VLA at 1.5 GHz a bright core with two hotspots.

In this thesis, a high-resolution observation of PKS 1451-375 with TANAMI at 8.4 GHz is analyzed as well as an observation with the VLA at 4.8 GHz. TANAMI is a VLBI program that uses antennas in the southern hemisphere which makes it the only VLBI program that can observe south of -30° . The observation with TANAMI was triggered due to a rise in flux observed by the Fermi satellite. The lightcurve from Fermi shows no prominent flux with the exception of a flare in October 2012. The TANAMI observation shows a bright core with a jet in south-western of 5 mas in length while the VLA observation shows a bright core with a one-sided jet and two hotspots in opposite directions from the core which is the typical morphology for a FR 2 galaxy.

A model fit analysis shows that the jet is nearly conical and the geometry is constant over both observations with a power-law index of $l = 0.960 \pm 0.033$ between the size of the components and the distance to the core. The brightness temperature gradient shows also a power-law with indices of $s_{TANAMI} = -3.46 \pm 0.14$ for the TANAMI observation and $s_{VLA} = -1.34 \pm 0.50$ for the VLA observation where $s = l + n + b(1 - \alpha)$ composed of the power-law index l for the jet geometry, n for the particle density, b for the magnetic field and α the spectral index. This suggests that a change in the jet happens and either the magnetic field index, the particle density index or the spectral index changes, assuming all are power-laws. The core of the TANAMI observation shows with $T_b = 2.1 \cdot 10^{11}$ K a brightness temperature the equipartition limit.

The inclination angle is estimated with the jet-to-counterjet flux density ratio of the TANAMI observation to an upper limit of $\phi < 22.5^\circ$ and with a method by comparing the apparent opening angle to a sample of similar sources to a lower limit of $\phi_{SW} > 52.5^\circ$ and $\phi_{NE} > 32.1^\circ$ for the two hotspots. Although the two results are not consistent, which could be the result of too small estimated hotspot sizes, it seems that PKS 1451-375 does not have the small inclination angles like blazars.

Contents

Zusammenfassung	iii
Abstract	v
1 Scientific Context	1
1.1 Active Galactic Nuclei	1
1.1.1 Unification model	3
1.1.2 Radiation processes	3
1.1.3 Brightness temperature	7
1.1.4 Doppler boosting	8
1.2 Very Long Baseline Interferometry	10
1.2.1 Very Large Array	13
1.2.2 TANAMI	13
2 Previous Research on PKS 1451-375	17
2.1 Morphology	17
2.2 Spectral Analysis	19
2.3 Gamma-Ray Detections	19
3 Data Analysis	22
3.1 <i>Fermi</i> /LAT	22
3.2 Imaging and Modelfitting in DIFMAP	22
3.2.1 TANAMI	23
3.2.2 VLA	24
4 Discussion	33
4.1 PKS 1451-375 in the TANAMI sample	33
4.2 Jet Orientation	33
4.3 Hotspots	34
4.4 Brightness Temperatur Gradients	37
5 Conclusion and Outlook	43
Bibliography	44
Acknowledgments	46
Declaration of Authorship	48

1 Scientific Context

1.1 Active Galactic Nuclei

Active galactic nuclei (AGN) are compact regions in the center of their host galaxies. They are among the most luminous objects found in the universe and emit radiation in the whole electromagnetic spectrum. Proposed by Salpeter (1964), the source of this strong radiation is accretion onto a supermassive black hole in the center of a disc of matter. Some of these sources show a relativistic jet perpendicular to the accretion disc.

AGN were discovered as individual phenomena starting in the early 20th century. Since Antonucci (1993) proposed a unifying model, the different types of AGN are seen as the different manifestation of the same underlying physical model. In this section, a brief overview of the different types of AGN is given. Furthermore, radiation processes are presented, as well as different properties of AGN.

The following classification of different AGN, adopted from Beckmann and Shrader (2012), is mainly based on the following parameters. The spectrum with the presence or absence of absorption lines, the morphology, the radio loudness and the luminosity. With the radio flux density S_r and the optical flux density S_o , the radio loudness R_{r-o} is defined by Kellermann et al. (1989) as

$$R_{r-o} = \frac{S_r}{S_o}.$$

If $0.1 < R_{r-o} < 1$, an AGN is called radio-quiet and if $R_{r-o} > 10$, an AGN is called radio-loud.

Seyfert galaxies

Seyfert galaxies differ from nonactive galaxies with a bright, point-like center. They are radio quiet and can be classified by their spectrum into Seyfert 1 and Seyfert 2. Seyfert 1 galaxies show broad allowed lines and narrow forbidden lines. Seyfert 2 galaxies show also narrow forbidden lines but in contrast to Seyfert 1 no broad lines and a weaker continuum, as well as absorption lines from their host galaxy.

Quasars

Quasars (quasi-stellar radio sources) are point like sources with strong radio emission. They have similar spectra as Seyfert galaxies, but weaker narrow lines and weaker absorption lines from their host galaxy. Quasars with lower radio luminosity were named QSOs (quasi-stellar objects) but the different terms are used mostly synonymous today.

Radio galaxies

Radio galaxies are mostly elliptical galaxies with a bright center but in contrast to Seyfert galaxies, they show strong radio emission with a jet. Their optical spectra

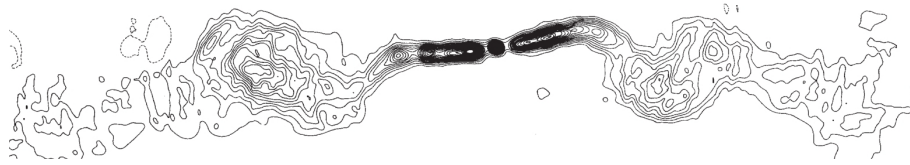


Figure 1.1: 3C 449, a typical FR 1 galaxy, observed with the VLA at 1.4 GHz. A bright central region with a bright jet that ends in plumes is visible. From: Perley et al. (1979).

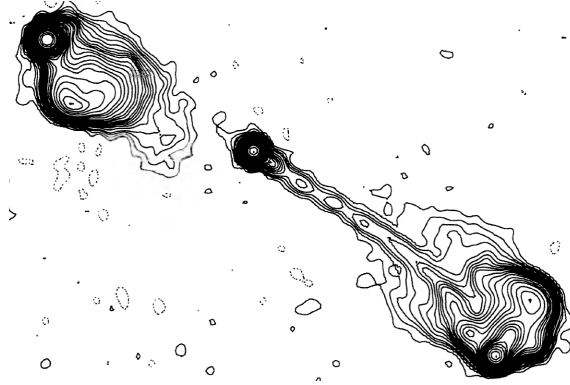


Figure 1.2: 3C 175, a typical FR 2 galaxy, observed with the VLA at 4.9 GHz. A bright central region with a jet in one direction is visible, as well as two bright radio lobes. From: Bridle et al. (1994).

are similar to Seyfert galaxies and analog they can be classified as narrow-line radio galaxies (NLRG) and broad-line radio galaxies (BLRG). Additionally, a classification of their morphology is possible. Fanaroff-Riley type 1 (FR 1) galaxies show a dominant nucleus with two asymmetric jets ending in plumes. Fanaroff-Riley type 2 (FR 2) galaxies have a less prominent core and often only one-sided jets ending in bright radio lobes where the jet hits the intergalactic medium. FR 2 galaxies are more luminous than FR 1.

Fig. 1.1 and 1.2 show typical FR 1 and FR 2 galaxies.

Blazars

Blazars are compact and strong radio sources with a highly variable spectrum. In regard to their spectrum, they can be divided into the sub-classes optically violent variables (OVVs), BL Lacertae objects (BL Lacs) and flat-spectrum radio quasars (FSRQs). OVVs and FSRQs show broad emission lines while BL Lacs have none. FSRQs are more luminous than BL Lacs and OVVs are less luminous than BL Lacs in the radio regime but stronger in the optical. The spectrum of a blazar shows typical in lower radio frequencies a steep power law that turn in to a flat spectrum at higher radio frequencies. This spectrum will be explained in the next section.

1.1.1 Unification model

According to Antonucci (1993) and Urry and Padovani (1995) all of the above classes of AGN can be described by one model.

Fig. 1.3 illustrate this model. In the center of an AGN, a supermassive black hole (SMBH) acts as the central engine. The surrounding area can be distinguished in four parts. A accretion disk with high particle density at a distance of about 10^{-3} pc, a broad line region (BLR) at 0.01 pc up to 0.1 pc, a dusty torus at 1 pc up to a few 10 pc and a narrow line region (NLR) at 100 pc up to 1000 pc. Additionally, radio-loud AGN form a jet perpendicular to the plane of the accretion disc and the torus.

According to the unification model, AGN can be described by only the viewing angle, the radio loudness and the luminosity. This relation is also illustrated in Fig. 1.3. The top half of the image displays radio loud AGN while radio quiet ones are in the bottom half. Different luminosities are illustrated by placing all high power AGN on the right side of the figure and low power AGN to the left side. Varying observation angles are shown by the different eyes of the observer.

If the jet of a radio-loud AGN points directly to the observer, it is seen as a blazar. FR 1 galaxies are low power radio-loud AGN observed at a higher angle and FR 2 are high power radio-loud AGN. Both are subdivided into BLRG and NLRG, dependent on the observation angle. Observing a BLRG, the NLR as well as the BLR are in the line of sight so broad allowed lines as well as narrow forbidden lines are visible in their spectrum. If the line of sight is nearly perpendicular to the jet, the BLR is hidden behind the dusty torus and therefore the broad lines are not visible in the spectrum.

In this model, BL LAC objects seem to be the rotated counterpart to FR 1 galaxies and FSRQ the counterpart of FR 2 galaxies. Therefore, observing a BL LAC object, a bright core with extended unbeamed emission around the core is expected and for FSRQ a bright core with one or two hotspots very close to it, due to the small inclination angle.

The bottom half of Fig. 1.3 shows the low power and radio-quiet Seyfert galaxies. Analog to BLRG and NLRG they are subdivided into Seyfert 2 where only the NLR is seen by the observer and Seyfert 1 where the NLR, as well as the BLR, are visible.

Table 1.1 summarizes this classification.

1.1.2 Radiation processes

The discovery of AGN and their extreme power raise the question of the nature of this strong radiation. The spectral energy distribution (SED) for a blazar is mostly flat with a typical double hump structure. The origin of the low-energy hump is understood as synchrotron radiation from mostly electrons and the high-energy hump a result of inverse Compton scattering. However, it is still unclear which particles contribute to the inverse Compton effect. Current models suggest also leptonic processes together with hadronic processes.

In the following section, synchrotron radiation, the most important process in

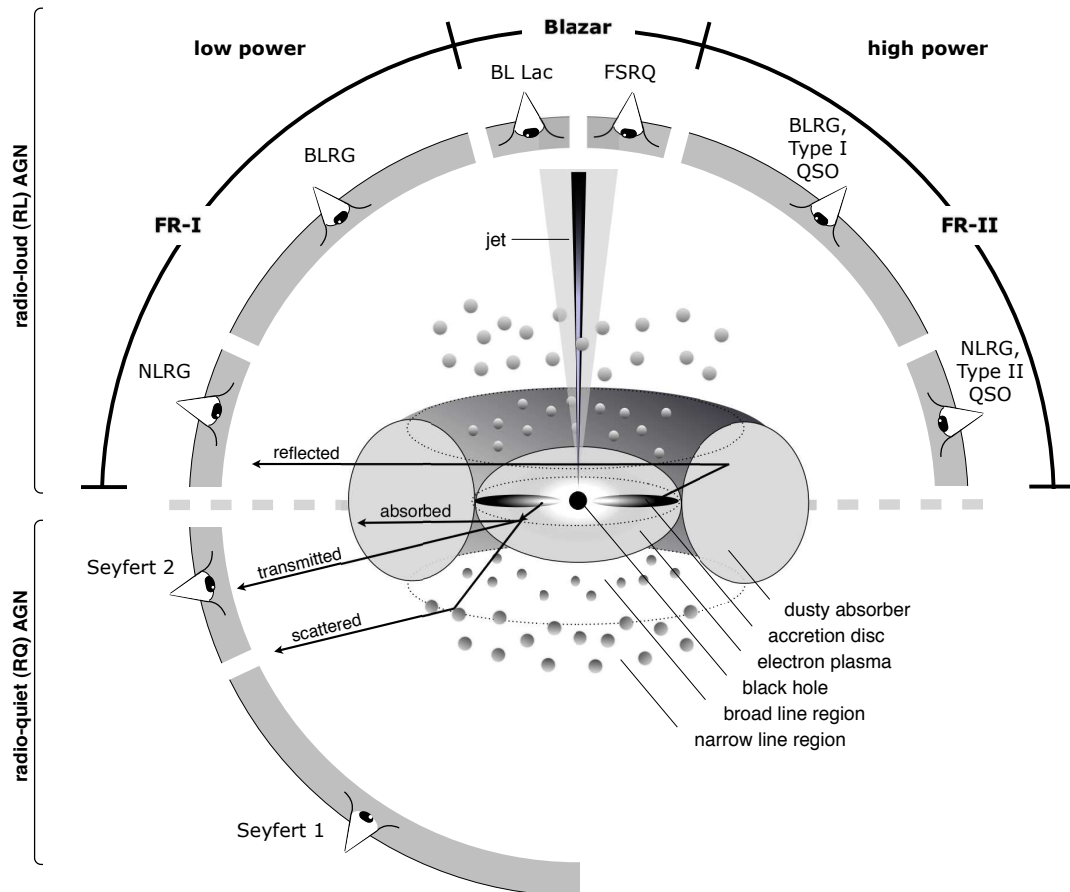


Figure 1.3: Illustration of the unification model by Beckmann and Shrader (2012). The center shows a simplified AGN model divided into radio-loud AGN in the top half and radio-quiet AGN in the bottom half. Objects with high luminosity are placed in the right side of the figure and objects with low luminosity in the left side. Different observation angles are illustrated by the different eyes of an observer.

Type	Radio Loudness	Emission Lines	Luminosity	Jet	Morphology
BL Lac	loud	-	low	yes	compact
FSRQ	loud	broad+narrow	high	yes	compact
BLRG	loud	broad+narrow	low	yes	FR 1
	loud	broad+narrow	high	yes	FR 2
NLRG	loud	narrow	low	yes	FR 1
	loud	narrow	high	yes	FR 2
Seyfert 1	quiet	broad+narrow	low	-	-
Seyfert 2	quiet	narrow	low	-	-
QSO (1)	quiet	broad+narrow	high	-	-
QSO (2)	quiet	narrow	high	-	-

Table 1.1: Summary of the classification of the different types of AGN. The top half shows the radio-loud AGN and the bottom half the radio-quiet AGN with no jet. Credit: Matthias Kadler.

the low-energy range, will be explained by following the textbook of Rybicki and Lightman (1979) for one emission region with an electron power-law population.

Synchrotron Radiation

Accelerated charge emits electromagnetic radiation, in case of relativistic electrons accelerated by a magnetic field this is called synchrotron radiation. The motion is described by the Lorentz-Force

$$\frac{d}{dt}(\gamma m \vec{v}) = \frac{e}{c}(\vec{v} \times \vec{B})$$

where e and m are the charge and rest mass of the particle, \vec{v} is the velocity and $\gamma = \sqrt{1 - \beta^2}^{-1}$ the Lorentz-factor, with $\beta = \frac{v}{c}$, where c is the speed of light. This leads to a helical motion around the B-field line. The emitted power is described by Eq. 1.1.2, also known as Larmor's formula.

$$P = \frac{dE}{dt} = \frac{q^2 \dot{v}^2}{4\pi c^3} \int \sin^2 \theta d\Omega = \frac{2q^2 \dot{v}^2}{3c^3}$$

The assumptions of an isotropic velocity distribution, relativistic electrons, and a messy derivation lead to the average emitted power

$$\langle P \rangle = \frac{4}{3} \beta^2 \gamma^2 c \sigma_T u_B$$

with the Thomson cross section $\sigma_T = (8\pi e^2)/(3m^2 c^4)$ and the magnetic field energy density $u_B = B^2/(8\pi)$. Because the mass scales with a power of -2 , Eq. 1.1.2 suggests that particles with a high mass are negligible and only the contribution of electrons is crucial. However, there are also models that take hadronic contributions into account (Mannheim (1993)).

For an electron distribution $n(\gamma)$, the power spectrum is obtained by weighting the power of each electron.

$$P_\nu = \int_1^\infty P_\nu(\gamma) n(\gamma) d\gamma$$

In case of non-thermal synchrotron radiation with a power-law distribution for the electrons,

$$n(\gamma) d\gamma = n_0 \gamma^{-p} d\gamma,$$

the power distribution reads

$$P_\nu = \frac{4}{3} \beta^2 \gamma^2 c \sigma_T U_B \phi_\nu(\gamma).$$

Here, the shape of the distribution is described by the function $\phi_\nu(\gamma)$ that is normed to one. By assuming that photons are only emitted at one characteristic frequency ω_c , $\phi_\nu(\gamma) \sim \delta(\nu - \omega_c)$. Each individual electron spectrum peaks at a specific frequency and together they add up to

$$P_\nu = \frac{2}{3} c \sigma_T n_0 \frac{U_B}{v_L} \left(\frac{\nu}{v_L} \right)^{-\frac{p-1}{2}}.$$

The emitted spectrum follows a power-law $P_\nu \propto \nu^{-\alpha}$, with the spectral index $\alpha = \frac{p-1}{2}$.

The spectrum of a blazar, composed of the steep power-law at low frequencies and a flat spectrum at higher radio frequencies, is a result of the inclination angle. In Fig. 1.4, the observer looks directly into the jet. The jet, consisting out of many single emission regions, emits a flat spectrum that is composed of the beamed emission of each region. The unbeamed extended emission produces the steep part of the spectrum. In Sec. 1.1.4, the effect of boosted emission regions and beamed emission will be explained more in detail.

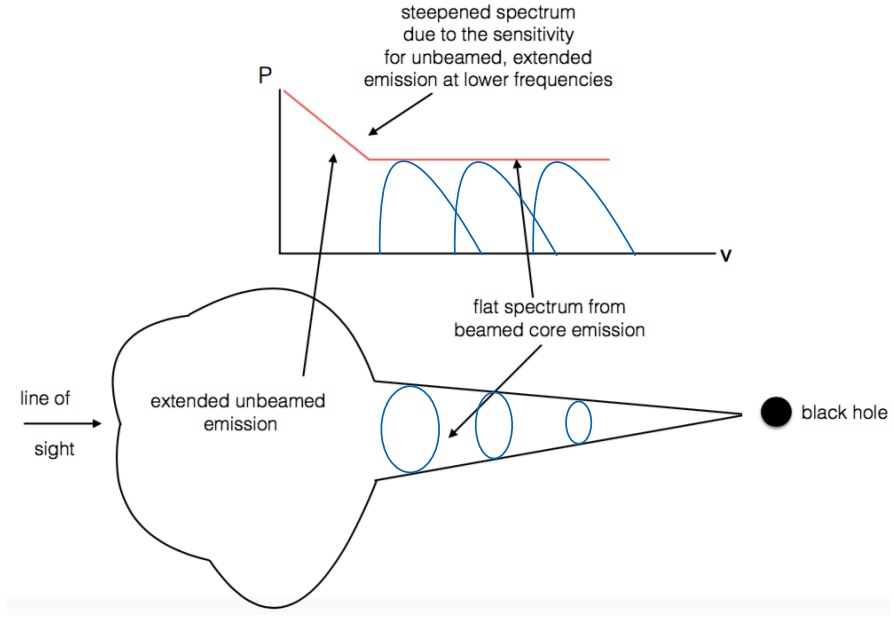


Figure 1.4: The radio spectrum of a blazar. The observer looks directly in the jet. The spectrum is composed of the unbeamed emission regions producing a steep power-law spectrum in the low radio frequencies and of the beamed emission of the many emission regions of the jet producing a flat spectrum in higher radio frequencies. From Burd (2017).

1.1.3 Brightness temperature

The brightness-temperature of an elliptical Gaussian component is defined by Kovalev et al. (2005) as

$$T_b = \frac{2 \ln(2) S \lambda^2 (1+z)}{\pi k \Theta_{maj} \Theta_{min}}. \quad (1.1)$$

S is the flux density of the component, λ the wavelength of the observation, z the redshift, k the Boltzmann constant and Θ_{maj} and Θ_{min} the Full Width at Half Maximum (FWHM) of the component along the major and minor axis.

Assuming, synchrotron emission leads to the measured brightness temperature, there seems to be a natural limit for T_b . The electrons, producing the synchrotron emission, can interact with photons by inverse Compton scattering. If these electrons are the synchrotron electrons themselves, the process is called synchrotron self-Compton (SSC). The energy losses of electrons due to inverse Compton scattering can be so high that the electrons get cooled significantly and can not contribute to the synchrotron emission anymore. According to Kellermann and Pauliny-Toth (1969), the luminosity of inverse Compton L_C is proportional to the energy density of the radiation field U_{rad} and the luminosity of the synchrotron radiation L_S is proportional to the energy density of the magnetic field U_B . This leads to an expression for the ratio between inverse Compton and synchrotron emission,

$$\frac{L_C}{L_S} = \frac{U_{rad}}{U_B} = \frac{1}{2} \left(\frac{T_b}{10^{12}} \right)^5 \nu_c \left[1 + \frac{1}{2} \left(\frac{T_b}{10^{12}} \right)^5 \nu_c \right]$$

where ν_c is the upper cutoff frequency in MHz. For $\nu_c = 10^5$ and $T_b < 10^{11}$ K, $L_C/L_S < 1$ but for higher brightness temperatures than 10^{12} K, $L_C/L_S \propto T_b^{10}$ and therefore only very little synchrotron emission takes place compared to inverse Compton. These catastrophic losses in inverse Compton are called the inverse Compton catastrophe. Then the brightness temperature decreases to 10^{11} K $\leq T_b \leq 10^{12}$ K until $L_C/L_S = 1$ which is called equipartition. This state can last much longer than the inverse Compton catastrophe, for example, if the maximum brightness temperature is at 1 GHz, for $T_b = 10^{11}$ K the half life the electrons is about 10^4 years compared to only 1 day for $T_b = 10^{12}$ K.

However, due to Doppler boosting higher brightness temperatures than the given limits can be measured.

According to Kadler et al. (2004) the brightness-temperature along a jet can be described by a power-law $T_b \propto r^s$, where r is the distance along the jet, if one makes the following assumptions:

$$d \propto r^l, n_e \propto r^n, B \propto r^b.$$

The diameter of the jet d , the particle density n_e and the magnetic field B can all be described by power-laws with the power-law indices l , n and b . Then

$$T_b \propto r^s \text{ with } s = l + n + b(1 - \alpha) \quad (1.2)$$

where α is the spectral index.

T_b can also be described by a power-law of the jet diameter d and the power-law index s_d :

$$T_b \propto d^{s_d} \text{ with } s_d = 1 + \frac{n + b(1 - \alpha)}{l} = \frac{s}{l}. \quad (1.3)$$

Blandford and Königl (1979) and Königl (1981) gave typical values for the power-law indices l , n , b and α as listed in table 1.2 together with the resulting s from Kadler et al. (2004).

1.1.4 Doppler boosting

Highly relativistic motion in the jet and a small inclination angle lead to an effect called Doppler boosting. If a light emitting object moves towards the observer, the particles are boosted and the radiation is beamed. Therefore the object appears to have a higher flux density than the same object at rest. On the other hand, the flux

	Blandford and Königl (1979)	Königl (1981)
l	1	1
n	-2	$-0.6 \geq n \geq -2$
b	-1	$-1 \geq b \geq -2$
α	-0.5	$0 \geq \alpha \geq -1$
s	-2.5	$-1.4 \geq s \geq -3$

Table 1.2: Typical values for the power-law indices for the T_b -gradient of a jet given in Blandford and Königl (1979) and Königl (1981) together with the resulting s from Kadler et al. (2004).

density of an object moving away from the observer is attenuated. If this effect is strong enough, an AGN with symmetrical jets in two directions can appear to have only a one-sided jet. Additionally, the spectrum is also blue shifted if the object moves towards the observer and red shifted if it moves away.

Following the textbook of Rybicki and Lightman (1979), the Doppler factor D of a relativistic jet is defined as

$$D = \frac{v_{obs}}{v_{em}} = \frac{\sqrt{1 - \beta^2}}{1 - \beta \cos(\phi)}$$

where $\beta = \frac{v}{c}$ and ϕ is the inclination angle. For speeds near c , the Doppler factor can become very large.

One can show that $S_\nu/(v)^3$ is a Lorentz invariant. For an object with a power law spectrum ($S(v) \propto v^{-\alpha}$) this leads to

$$I(v_{obs}) = D^{3+\alpha} I(v_{em})$$

where $I(v_{obs})$ is the observed intensity and $I(v_{em})$ the emitted intensity.

Applying this to a source that emits two emitting regions in opposite directions, the ratio of their observed flux density is

$$R = \frac{S_{jet}}{S_{counterjet}} = \left(\frac{1 + \beta \cos(\phi)}{1 - \beta \cos(\phi)} \right)^p \quad (1.4)$$

with $p = 3 + \alpha$ for individual components and $p = 2 + \alpha$ for a contentious jet. R is called the jet-to-counterjet-ratio and even for low relativistic speeds it can reach high values and therefore let a two-sided jet appear to be one-sided due to sensitivity limitations of the used telescope.

1.2 Very Long Baseline Interferometry

To resolve the innermost parts of AGN, a high angular resolution is needed and the concept of interferometry is used, where several telescopes get linked together. This section shows the needs for this technique and presents the basics of radio interferometry following the textbook of Burke and Graham-Smith (2010). Furthermore, a brief overview of the two radio interferometers used in this thesis is given.

The angular resolution for a single dish telescope is given by the Rayleigh criterion

$$\Theta \approx 1.22 \frac{\lambda}{D}$$

where λ is the wavelength of the observed radiation, D is the diameter of the dish and the factor of 1.22 is an approximation of the first Bessel's function of the incoming signal becoming zero. The largest fully steerable radio telescopes are the Robert C. Byrd Green Bank Telescope (GBT) in Green Bank (US) and the Effelsberg 100-m Radio Telescope in Effelsberg (Germany) with diameters of about 100 m. Observations with those telescopes at $\nu = 8.4$ GHz yield to an angular resolution of $\Theta_{\text{Effelsberg}} = 89.81$ as. However, to study the inner parts of AGN the resolution has to be orders of magnitudes higher.

For an interferometer, the resolution is given by the largest distance between two single-dish telescopes. One of those connection lines is called baseline \vec{b} . This leads to very high angular resolutions, i.e. the longest baseline of the TANAMI which is located in the southern hemisphere is about 10244 km which results in a resolution of $\Theta_{\text{TANAMI}} = 0.88$ mas at $\nu = 8.4$ GHz.

The concept of a radio interferometer will be explained by a two-element Michelson interferometer, shown in Fig. 1.5. The two single-dish telescopes observe a source in the direction given by the vector \vec{s} .

The received power of a telescope dish is given by

$$P_{\text{rec}} = \int_0^\infty d\nu A_{\text{eff}}(\nu) S(\nu)$$

with the effective area of the dish A_{eff} and the flux density $S(\nu)$ which is the integral of the brightness distribution $B(\nu, \vartheta, \varphi)$ of the source over the whole sky $S(\nu) = \int d\Omega B(\nu, \vartheta, \varphi)$. The incoming signal arrives at the second telescope with a geometrical delay τ_g and an additional instrumental delay τ_i can be added. In a correlator, the two signals get correlated and the cross-correlation function $R(\tau)$ is given by the time-averaged product over the two amplitudes measured by the antennas $x(t) = v_1 \cos(2\pi\nu t)$ and $y(t - \tau) = v_2 \cos(2\pi\nu t)$ which is delayed by τ :

$$R_{xy}(\tau) := \langle x(t) y(t - \tau) \rangle = S A_{\text{eff}}(\vec{s}) \cos(2\pi \vec{b}_\lambda \vec{s})$$

where \vec{b}_λ is the baseline measured in wavelengths.

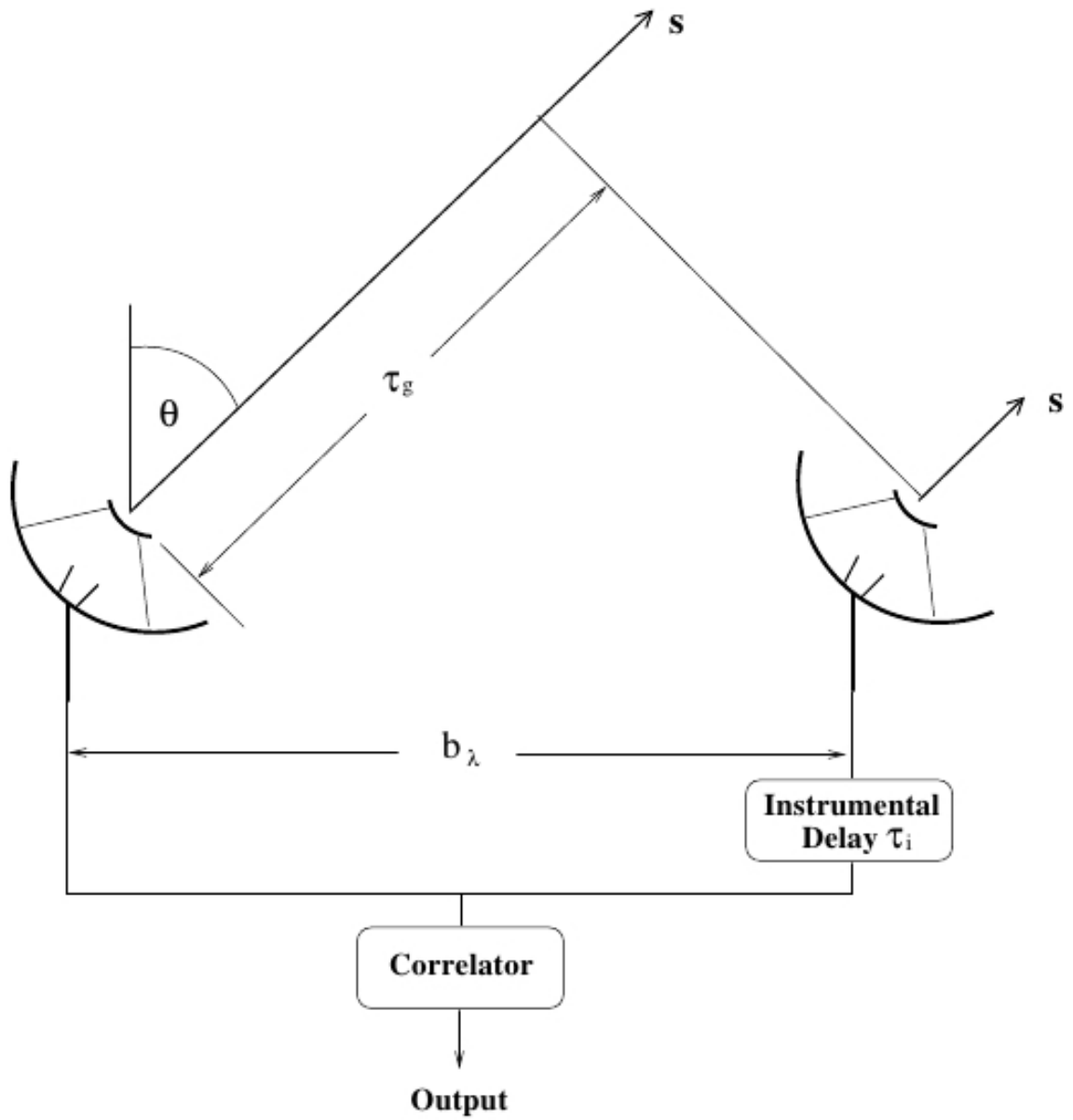


Figure 1.5: Concept of a two element radio interferometer. The individual dishes are separated by the baseline b_λ and observe an object in the direction of \vec{s} . With the geometrical delay τ_g and an additional instrumental delay τ_i , the data is collected after the two signals run through the correlator. From: Burke and Graham-Smith (2010).

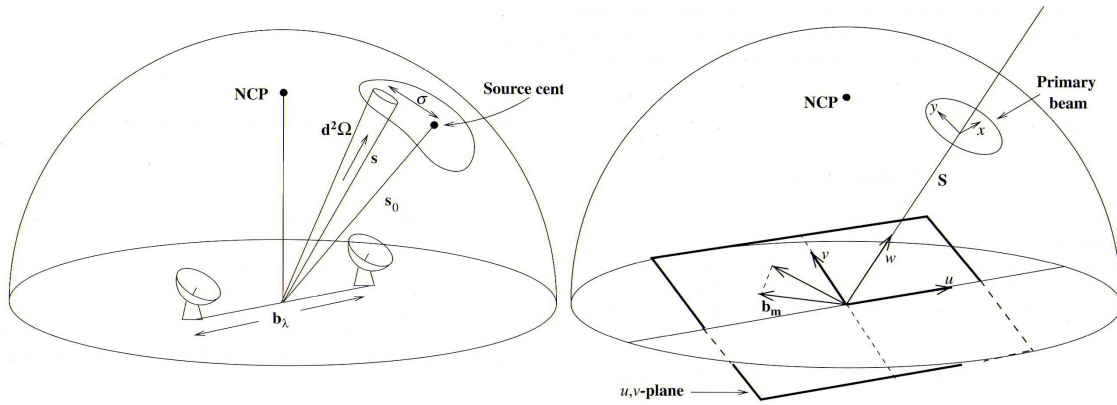


Figure 1.6: On the left, the observation of an extended source under the direction of \vec{s} and the solid angle $d\omega$. Then the time delay only depends on σ . On the right, the concept of the (u, v) -plane and is shown. From: Burke and Graham-Smith (2010).

Fig. 1.6 (left) shows the observation of the source under the direction $\vec{s} = \vec{s}_0 + \vec{\sigma}$. For $\tau_i = \tau_g$, \vec{s}_0 is called the phase tracking centre. When the geometrical delay is compensated with an instrumental delay, the measured time delay only depends on $\vec{\sigma}$. Then, the complex visibility function V of the brightness distribution $B_v(\vec{\sigma})$ for one baseline is given by

$$V = \int A_{eff}(\vec{\sigma}) B_v(\vec{\sigma}) \exp(i2\pi \vec{b} \cdot \vec{\sigma}) d\Omega$$

with the solid angle $d\Omega$ of the source.

Fig. 1.6 (right) introduces the (u, v) -plane. The coordinate system (u, v, w) is defined by \vec{s}_0 which defines the w direction and since $\vec{\sigma}$ sits perpendicular on \vec{s}_0 , $w = 0$ and $\vec{\sigma}$ lies only in the (u, v) -plane. The visibility function then becomes

$$V(u, v) = \int A_{eff}(l, m) B_v(l, m) \exp(i2\pi(ul + vm)) \frac{dl dm}{\sqrt{1 - l^2 - m^2}}$$

where l, m, n are the direction cosines of \vec{s} and therefore $d\Omega$ becomes $\frac{dl dm}{\sqrt{1 - l^2 - m^2}}$.

It is the Fourier transform of the brightness distribution B_v of the source of interest and phase and amplitude of the complex visibility function are the observables in radio interferometry. The problem in radio interferometry is the impossibility to cover the entire (u, v) -plane in an observation. This correspondent to a loss of Fourier components in the image and is, therefore, the challenge in image synthesis to compensate for that. Each baseline corresponds to a pair of points in the (u, v) -plane, so observing with more antennas increases the (u, v) -coverage. Additionally, observing longer, or at different times creates half ellipses in the (u, v) -plane due to Earth's rotation which is called Earth rotation synthesis. Fig. 1.7 shows the (u, v) -coverage of the Very Large Array (VLA) at four different declinations. While the observation a $\delta = 0^\circ$ does not take advantage of Earth's rotation synthesis, observing

at higher declination increases the (u, v) -coverage drastically by producing ellipses in the (u, v) -map.

The research done in this thesis made use of two radio interferometers, the Karl G. Jansky Very Large Array (VLA), which is a compact array and TANAMI, a very long baseline interferometer. In a compact array, the antennas are connected to a correlator while a direct connection is not possible for a very long baseline interferometer where the antennas are placed several thousand kilometers apart. Therefore the data gets recorded, shipped to one location and then correlated. In return, a very long baseline interferometer offers much longer baselines and a much higher angular resolution.

1.2.1 Very Large Array

The VLA is located in New Mexico and consists of 27 identical antennas with 25 m in diameter arranged in a Y-shape form (Perley et al. (2011)). Due to the possibility of moving the antennas on a rail system, different configurations with baselines reaching from 1 km to 36 km are achievable. Fig. 1.8 shows the VLA in D configuration with baselines up to 1 km. Since a modification, the array is named Karl G. Jansky Very Large Array. Observations between 1 GHz and 50 GHz are possible in continuum mode or channel mode.

1.2.2 TANAMI

The Tracking Active Galactic Nuclei with Austral. Milliarcsecond Interferometry (TANAMI) is a multiwavelength program observing a sample of bright AGN. This section follows Ojha et al. (2010), Kadler et al. (2015) and Müller et al. (2017). The location of TANAMI in the southern hemisphere makes it the only VLBI program that is capable of observing south of declination -30° . Observations are possible at 8.4 GHz and 22 GHz, which makes it possible to get spectral indices for the core as well as bright jet components. The chief incentive for TANAMI was the launch of the Fermi Space Telescope and therefore get high-resolution VLBI observations and flux-density monitoring of new AGN candidates. Starting with a sample of 43 sources (Ojha et al. (2010)), it is now monitoring a variety of different AGN.

In recent years, a multiwavelength program has developed around TANAMI providing also NIR, optical, UV, X-ray and γ -ray coverage, made possible by a variety of collaborations, i.e. Fermi, Swift, XMM-Newton, INTEGRAL, Suzaku, REM, and TNG.

TANAMI uses several radio telescopes in Australia, including the six stations of the Australian Long Baseline Array (LBA). To increase the resolution, longer baselines are added with different stations outside of Australia. Table 1.3 gives an overview of the different antennas used in TANAMI and Fig. 1.9 shows the distribution of the stations over the southern hemisphere.

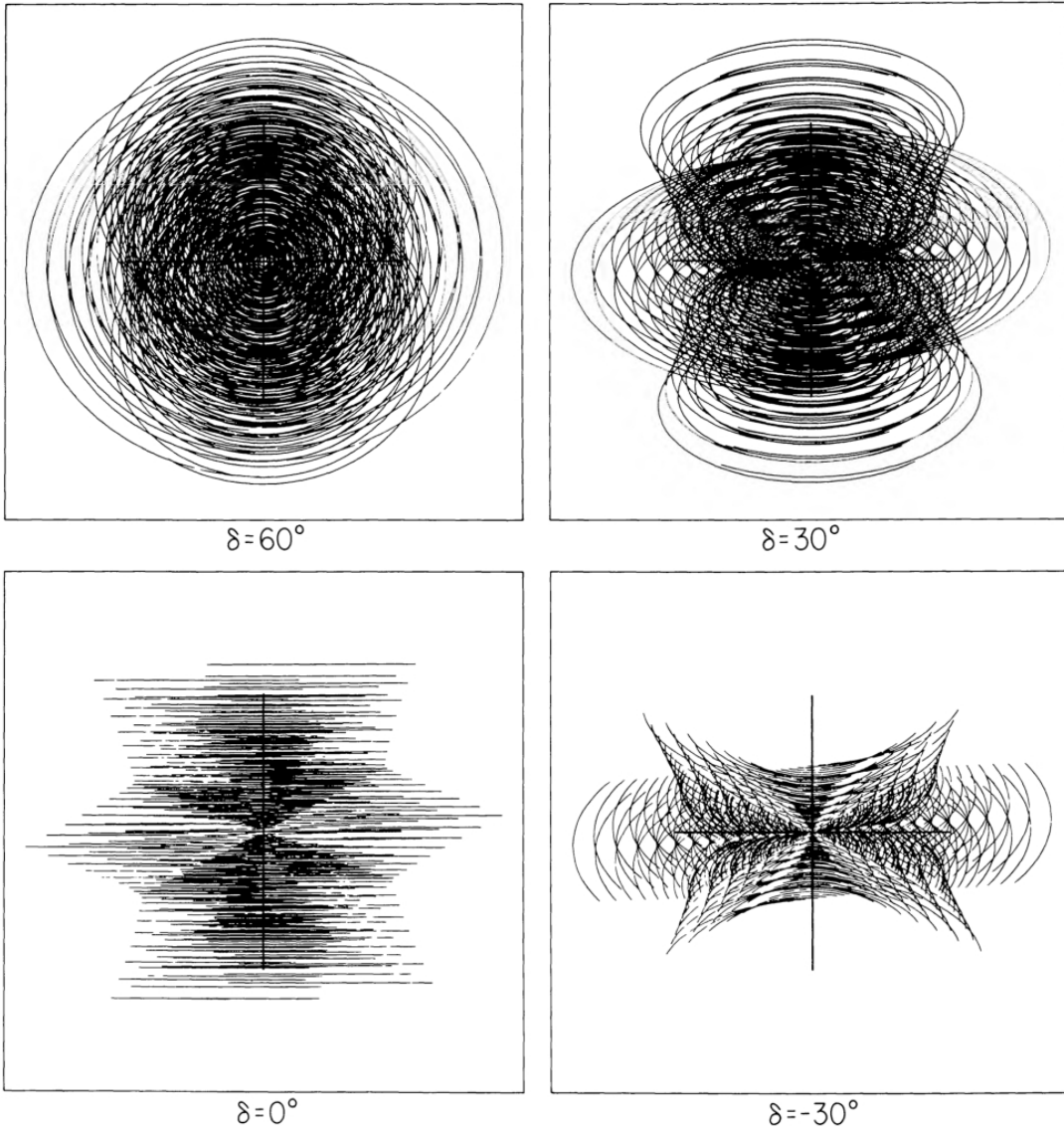


Figure 1.7: (u, v) -coverage of the Very Large Array at different declinations for an observation of 8 h. From: Thompson et al. (1980).



Figure 1.8: The Very Large Array in D configuration. From: Perley et al. (2011).

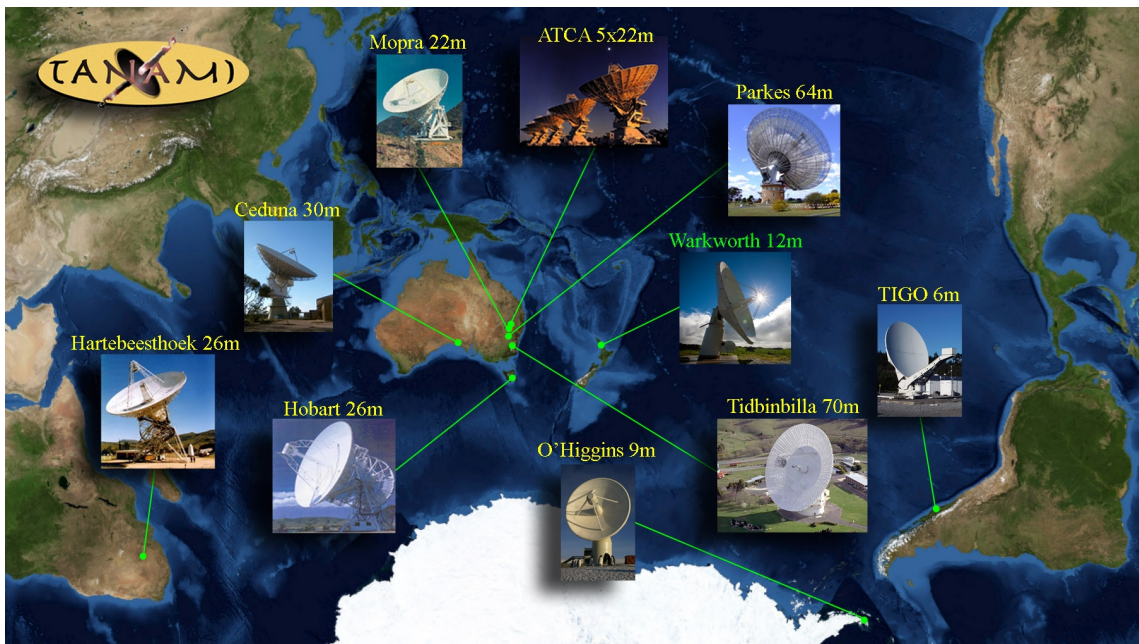


Figure 1.9: The TANAMI telescopes. Credit: M. Kadler & J. Wilms.

Telescope (Abbreviation)	Diameter [m]	Location
Parkes (PA)	64	Parkes, New South Wales, Australia
ATCA (AT)	5 x 22	Narrabri, New South Wales, Australia
Mopra (MP)	22	Coonabarabran, New South Wales, Australia
Hobart (HO)	26	Mt. Pleasant, Tasmania, Australia
Ceduna (CD)	30	Ceduna, South Australia, Australia
DSS ¹ 43	70	Tidbinbilla, ACT, Australia
DSS ¹ 45	34	Tidbinbilla, ACT, Australia
DSS ¹ 34	34	Tidbinbilla, ACT, Australia
Katherine (KE)	12	Katherine, Northern Territory, Australia
Yarragadee (YG)	12	Yarragadee, Western Australia, Australia
Hartebeesthoek ² (HH)	26	Hartebeesthoek, South Africa
O'Higgins ² (OH)	9	O'Higgins, Antarctica
TIGO ² (TC)	6	Concepcion, Chile
Warkworth (WW)	12	Auckland, New Zealand

Table 1.3: Telescopes of TANAMI, according to Müller et al. (2017). ACT stands for Australia Capital Territory.

¹ Operated by the Deep Space Network of the National Aeronautics and Space Administration. ² Operated by Bundesamt für Kartographie und Geodäsie (BKG).

2 Previous Research on PKS 1451-375

PKS 1451-375, also known as J1454-3747, was discovered with the Parkes Radio Telescope at 2.7 GHz and 5 GHz by Peterson and Bolton (1972a). It is described as a radio variable Quasi-Stellar Object (QSO) and a by spectroscopic observations in the optical regime a redshift of $z = 0.314$ could be determined by Peterson and Bolton (1972b).

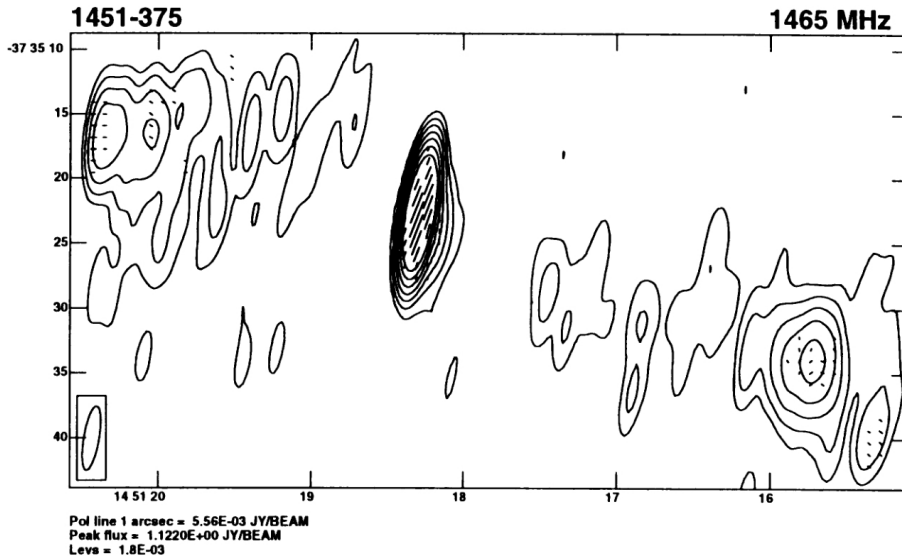


Figure 2.1: PKS 1451-375 at 1.465 GHz observed with the VLA. The polarisation of the magnetic field is indicated by small lines. From: Saikia et al. (1998).

2.1 Morphology

Due to the position of PKS 1451-375 (RA = 14h 54m 27.4s, DEC = -37d 47m 33s ¹), it can be observed with the VLA and observations at 5 GHz made in 1980 revealed a jet in south-western direction with a projected length of 17 kpc (Perley (1981), Bridle and Perley (1984)). The jet is classified as one-sided which is by definition a jet with a jet-to-counter-jet ratio in flux bigger than four.

Further observations at 1.465 GHz with the VLA (Saikia et al. (1998)) show two hotspots south-west and north-east of the bright core (see Fig. 2.1) which indicates an FR 2-like radio morphology. The map shows also the polarisation of the magnetic field in the core and at the two hotspots.

The first high-resolution image with milliarcsecond resolution was made in a 5 GHz prelaunch survey for the VLBI Space Observatory Programme (VSOP) using the Very Large Baseline Array (VLBA) in June 1996 (Fomalont et al. (2000)). It shows a compact object with some structure in western and south-western direction. A modelfit analysis relieved three components. The bright core with 2.146 Jy, a

¹<https://ned.ipac.caltech.edu>

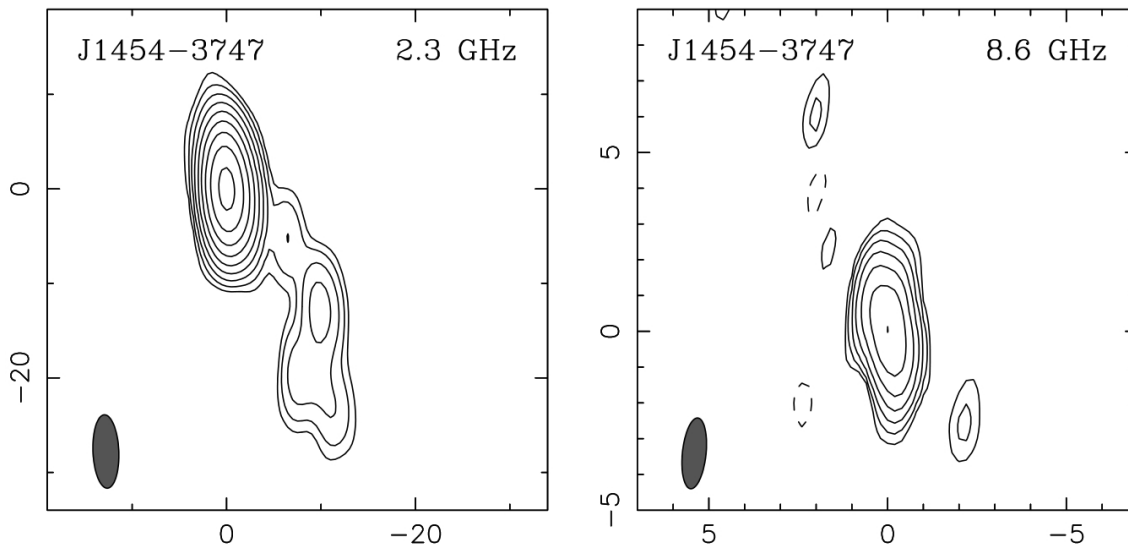


Figure 2.2: PKS 1451-375 at 2.3 GHz and 8.6 GHz observed with the VLBA. From: Pushkarev and Kovalev (2012).

component 6.7 mas south-west of the core with 0.095 Jy and one 13.0 mas south-west of the core with 0.037 Jy.

High-resolution images were also obtained with the VLBA+ network (consisting of the ten antennas of the VLBA and up to nine geodetic antennas all over the world to increase the resolution up to a factor of two compared to VLBA)² of the U.S naval observatory in a program observing radio reference frame sources (see Johnston et al. (1995) for more information). These images are available to the public³ and there are 19 epochs between January 1997 and May 2009 at 2 GHz and 8 GHz for PKS 1454-375. All of these images show a bright compact object. Some epochs indicate a jet-like structure in south-western direction, i.e. the newest 8.6 GHz image from May 14, 2009.

Similar observations were made by Pushkarev and Kovalev (2012) with VLBA data collected in December 2002 at 2.3 GHz and 8.6 GHz shown in Fig. 2.2. The 2.3 GHz image shows a compact core with a jet-like structure of 25 mas in a south-western direction. Three components are identified. The core with 0.918 Jy, a component 9.5 mas south-west of the core with 0.063 Jy and one 16.3 mas south-west of the core with 0.030 Jy. The 8.6 GHz image shows a compact source and a model fit analysis revealed two components. The core with 0.460 Jy and a component with 0.422 Jy 1.0 mas south-west of the core. The total flux is 1.02 Jy at 2.3 GHz and 0.88 Jy at 8.6 GHz.

All observations with a model fit analysis are summarized in table 2.1.

²<http://rorf.usno.navy.mil/RRFID/vlba+.html>

³<http://rorf.usno.navy.mil/rrfid.shtml>

	ν	Component	S	a_{maj}	Ratio	R	Θ
	[GHz]		[mJy]	[mas]		[mas]	[$^\circ$]
F	5	Core	2.146	0.5	< 0.6		
		1	0.095	4.6	< 0.15	6.7	-145
		2	0.037	7.3	0.27	13	-144
P	2.3	Core	0.918	2.2	0.34		
		1	0.063	0.10	1	9.5	-142
		2	0.030	2.5	1	16	-137
P	8.6	Core	0.460	0.43	1		
		1	0.422	0.25	1	1.0	-153

Table 2.1: All observations of PKS 1451-375 with a modelfit analysis. F stands for Fomalont et al. (2000) and P for Pushkarev and Kovalev (2012). ν displays the frequency of the observation, S of the given component, a_{maj} is the major axis, Ratio the ratio of the minor to the major axis, R and Θ are the polar coordinates with the core-component as the point of origin.

2.2 Spectral Analysis

The first spectral index analysis by Quiniento and Echave (1990) revealed a flat spectrum with spectral indexes $\alpha_{0.4}^{1.4} = -0.49$ between 0.4 GHz and 1.4 GHz, $\alpha_{1.4}^{2.7} = -0.07$ and $\alpha_{2.7}^5 = 0.32$. Similar results were measured by Massardi et al. (2008) in the Australia Telescope 20-GHz Survey with $\alpha_{4.8}^{8.6} = 0.14$ and $\alpha_{8.6}^{20} = -0.01$ which also indicates a flat radio spectrum. This implies that PKS 1451-375 is a blazar.

PKS 1451-375 was handled as a candidate for a damped Lyman- α -series (Chenagur and Kanekar (2000)) but no significant absorption was detected.

2.3 Gamma-Ray Detections

PKS 1451-375 was already observed by the Energetic Gamma Ray Experiment Telescope (EGRET) but no significant detection was made. Only an upper limit for the flux of photons above 100 MeV is given with $0.8 \text{ ph cm}^{-2} \text{ s}^{-1}$ for an observation period of about 14 days Fichtel et al. (1994).

The *Fermi* Gamma-ray Space Telescope (*Fermi*) equipped with the Large Area Telescope (LAT) detects photons in an energy range of 20 MeV to 300 GeV. Bastieri (2012) reports a brightest detection of PKS 1451-375 and a preliminary analysis estimated the daily flux above 100 MeV to $(1.2 \pm 0.4) \cdot 10^{-6} \text{ ph cm}^{-2} \text{ s}^{-1}$. Due to this activity, multiwavelength observations were strongly recommended by the Fermi LAT Collaboration. Since the detection, PKS 1451-375 is observed regularly and preliminary public data is available. Fig. 2.4 shows the weekly binned γ -ray lightcurve for

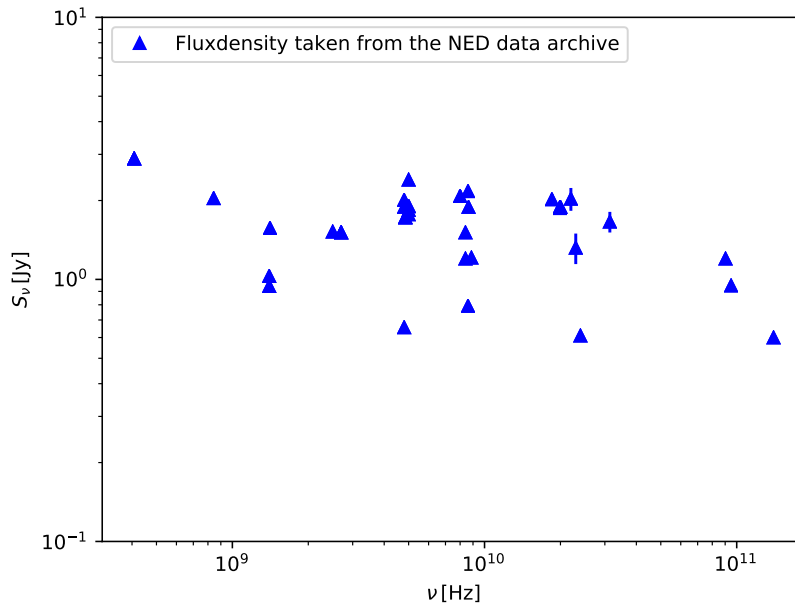


Figure 2.3: Spectrum of PKS 1451-375 from the NED-database (<https://ned.ipac.caltech.edu/>) in the range of 0.1 GHz to 100 GHz. A mostly flat spectrum is visible with a possible steepening at lower frequencies. This is consistent with the spectrum of a blazar as shown in Sec. 1.1.2 and suggests that this source is a blazar.

PKS 1451-375 in the time between October 2012 and February 2018.

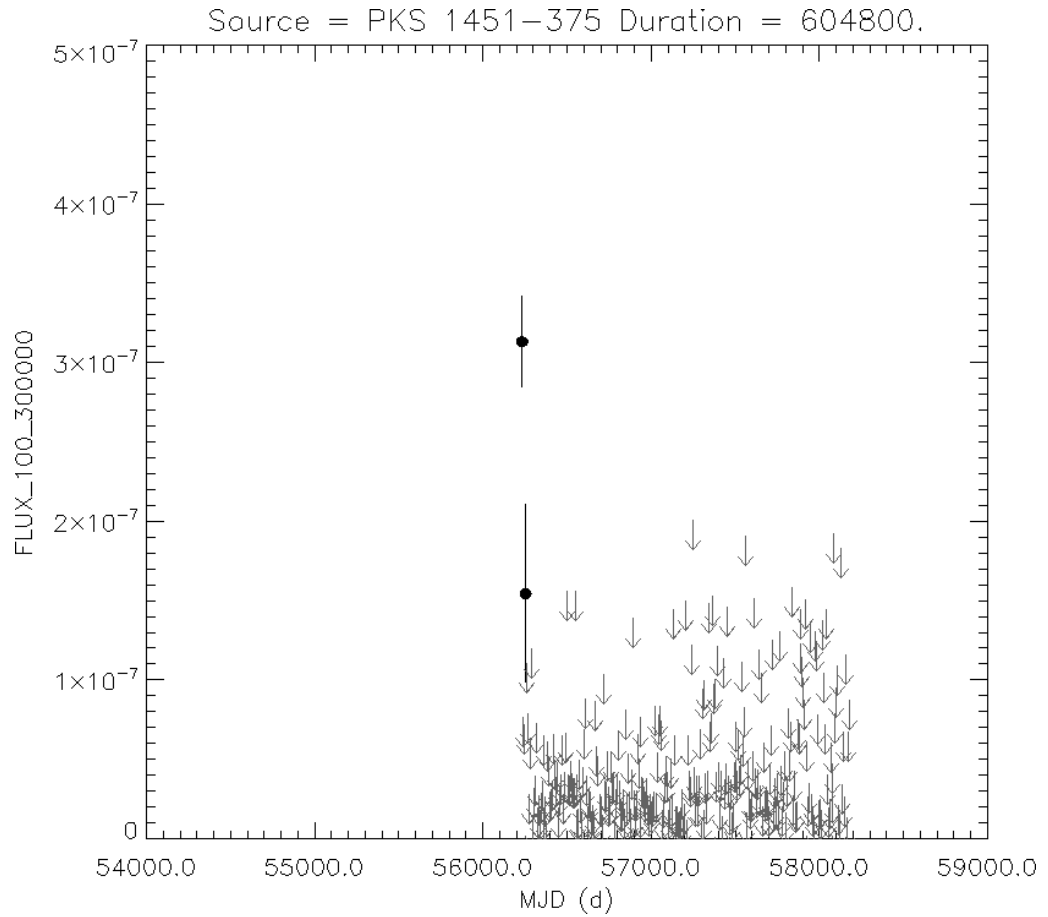


Figure 2.4: Public γ -ray lightcurve of PKS 1451-375 observed with *Fermi*/LAT in the energy range of 100 MeV to 300 GeV using weekly binning. Arrows show upper limits and the filled points detections together with their uncertainty. From: <https://fermi.gsfc.nasa.gov/ssc/data/>.

3 Data Analysis

The main part of this thesis is to image and modelfit a TANAMI observation of PKS 1451-375 obtained on August 17, 2013, and an observation of the same object obtained with the VLA on December 30, 2004. For this, the program DIFMAP developed by Shepherd (1997) is used. The data is already phase and amplitude calibrated which can be achieved with the Astronomical Image Processing System (AIPS). See Greisen (2003) for more information about the calibration process. In this section, a brief overview of the program DIFMAP is presented along with the analysis of the two observations. Furthermore, a more detailed look at the flare observed with *Fermi* is given, which is the reason for the observation of PKS 1451-375 with TANAMI.

3.1 *Fermi*/LAT

To investigate the γ -flare more in detail, the data collected with *Fermi*/LAT is further analyzed. The public available lightcurve (see Fig. 2.4) shows no detection before October 2012, when the high flux was measured.

Fig. 3.1 shows a dedicated Pass 8 lightcurves in the energy range between 100 MeV and 300 GeV. The top lightcurve shows the measured flux in the time between 2009 and 2017 with 30-day binning. In these eight years, the flux did not exceed $10^{-7} \text{ ph cm}^{-2} \text{ s}^{-1}$ with the exception of one data point in October, 2012 which matches the reported rise in flux in Bastieri (2012). The bottom lightcurve in Fig. 3.1 shows the same data with one-day binning in the time between early 2013 and late 2017. This is also apparent on the bottom lightcurve in 3.1 with one-day binning where the preliminary estimated daily flux of $(1.2 \pm 0.4) \cdot 10^{-6} \text{ ph cm}^{-2} \text{ s}^{-1}$ during the flare lies within the error of the highest data point. In this lightcurve, the flux drops after the flare roughly to its usual level and rises in November 2012 again, which could be another, less luminous flare.

3.2 Imaging and Modelfitting in DIFMAP

As shown in Sec. 1.2, the visibility is the Fourier transformed of the convolution of the brightness distribution on the sky and the effective area of the antenna, respectively the beam pattern. In an ideal observation, the (u, v) -plane is completely filled and therefore the recovery of the image would be simple. In reality, the (u, v) -coverage shows large amounts of gaps and a more complex calculation has to be done.

The following steps are based on Shepherd (1997) and the DIFMAP-cookbook⁴. DIFMAP uses the clean algorithm developed by Högbom (1974), which approximates the brightness distribution with point sources, to recover the image. First, the user starts with the so-called dirty image, which is a convolution of the intensity distribution with the dirty beam. The dirty beam is the Fourier transform of the

⁴<ftp://ftp.astro.caltech.edu/pub/difmap/difmap.html>

(u, v) -plane. Then, the user sets an area around the brightest spot in the dirty image. In this area, clean is allowed to set a δ -function as the point source, multiply it with the dirty beam and then subtracts the flux density of this point source from the dirty map. This process is repeated until the remaining flux in the dirty map is sufficiently small. Then the point source model is convoluted with a Gaussian clean beam to get the clean image.

After each individual step of the clean algorithm, a phase self-calibration is performed while amplitude self-calibration is only done if the data is already sufficiently cleaned and repeated with decreasing time intervals. Self-calibration uses the fact that the phase of 3 antennas and the amplitude of 4 antennas is conserved. See Jennison (1958) for more detailed information. This method is used to adjust the data to the model. The process of building the model with clean and adjusting the data with self-calibration is called hybrid imaging (Pearson and Readhead (1984)).

Instead of a model consisting out of many point sources, DIFMAP allows with the `modelfit` command to fit the data to a simpler model consisting out of elliptical Gaussian components. For each component of this model, a brightness temperature can be defined as shown in Sec. 1.1.3 and therefore the object can be studied in a more detailed way.

In DIFMAP it is possible to weight individual visibilities with a Gaussian taper before any cleaning is applied. There are two values to set. The Gaussian taper value sets how much the taper should fall and the UV radius at which radius the taper should fall to the Gaussian taper value. A tapered image is used to find possible extended structure in the image. The disadvantage is the loss of angular resolution due to the down-weighting of longer baselines.

According to Kovalev et al. (2005) the minimal resolvable size of a Gaussian component a_{lim} is given by

$$a_{lim} = b \sqrt{\frac{4 \ln 2}{\pi} \ln \left(\frac{SNR}{SNR - 1} \right)}$$

where b is the half-power beam size and SNR is the standard noise ratio which is given by $SNR = S/\sigma$ where S is the flux density of the component and σ the noise level in the area, where the component sits. If one axis of a component is smaller than a_{lim} it is considered as unresolved and a_{lim} can be used as an upper limit.

3.2.1 TANAMI

The observation of PKS 1451-375 with TANAMI was triggered due to the high measured flux with Fermi/LAT in October 2012. The observation with TANAMI at 8.4 GHz took place on August 17, 2013 and Fig. 3.2 shows the (u, v) -coverage.

Due to the nature of a very long baseline interferometer, the (u, v) -coverage is much poorer than for an observation with a compact array, i.e. the VLA. However, compared to other TANAMI observations the (u, v) -coverage is quite good. The data was imaged using clean and self-calibration in DIFMAP and the clean map is shown in Fig. 3.3.

The source shows a bright, point-like center and in a south-western direction, a jet-like structure approximately 5 mas in length, which is consistent with the previous observation of PKS 1451-375 as all VLBI observations showed a bright center and a few also a jet in south-western direction. A counter-jet is not visible. Imaging with a Gaussian taper did not reveal any extended structure and showed only the bright core.

In Fig. 3.4 the point-source model is replaced with Gaussian model components. Compared to the previous image the jet looks different and the noise level is higher due to the less accurate representation of the Gaussian components. However, the overall structure still remains the same with a bright core and a jet of approximately 5 mas in length. Only the component in the center was allowed to be elliptical while the components in the jet had to remain spherical. The components get bigger as the distance from the center increases as it is expected for a conical jet. The parameters of all components including the core-component are listed in table 3.1 together with the resolution limit and the brightness temperature that is calculated following Eq. 1.1. Since the resolution limit is always smaller than the major axis of any component, no adjustment is needed.

Component	$S_{8.4}$ [mJy]	R [mas]	Θ [deg]	a_{maj} [mas]	a_{lim} [mas]	Ratio	T_b [K]
Core	826	0	0	0.435	0.0617	0.372	$2.6 \cdot 10^{11}$
1	304	0.7101	-134.5	0.335	0.102	1	$6.1 \cdot 10^{10}$
2	72.5	2.534	-146.9	1.336	0.209	1	$9.2 \cdot 10^8$
3	8.46	4.585	-139.6	1.449	0.630	1	$9.1 \cdot 10^7$

Table 3.1: Gaussian components for the observation of PKS 1451-375 obtained with TANAMI. $S_{8.4}$ displays the flux at 8.6 GHz, R and Θ are the polar coordinates with the core-component as the point of origin, a_{maj} is the major axis, a_{lim} the resolution limit of the major axis, Ratio the ratio of the minor to the major axis, T_b the brightness temperature.

3.2.2 VLA

Additionally to the high-resolution observation with TANAMI, archival data of PKS 1451-375 collected with the VLA in A-configuration on December 30, 2004, at 4.8 GHz is imaged and model-fitted. Fig. 3.5 shows the clean map of this observation. The source has a bright center that segues into a jet, approximately 32 arcsec in length, that points in the same direction than the jet of the TANAMI observation.

Although this jet in south-western direction is not continuous at the whole of its length, it is much more prominent than in the observation by Saikia et al. (1998) in Fig. 2.1. The jet ends in a structure at approximately 32 arcsec from the center that is much brighter than most of the jet. In the opposite direction is no jet visible

but the same bright structure that is also apparent on the other side of the center but at a distance of approximately 25 arcsec from the center.

Fig. 3.6 shows the same observation, where parts of the point-source model (shown as crosses) are replaced with Gaussian components (shown as crossed circles). Not all point-source components were removed because, in regions outside the main structures like the core, the jet and the two bright regions, Gaussian components would become unphysical. Analog to the TANAMI observation, the image changes due to the less accurate model with Gaussian components, however the overall structure remains the same.

Tabel 3.2 lists all Gaussian components including the core together with the resolution limit and the brightness temperature. No component is smaller than the resolution limit. Following the jet in south-western direction, the components get bigger and the brightness temperature lower until component 7 when they get smaller again and have a higher brightness temperature. Component 12, 13 and 14 are the ones on the opposite side of the core.

Component	S _{4.8} [mJy]	R [arcsec]	Θ [deg]	a _{maj} [mas]	a _{lim} [mas]	Ratio	T _b [K]
Core	660	0	0	16.33	13.94	1	1.73 · 10 ⁸
1	4.57	0.3424	-151.9	178.1	168.2	1	1.01 · 10 ⁴
2	3.91	1.194	-143.0	519.3	182.0	1	1.01 · 10 ³
3	7.85	1.814	-134.9	490.1	128.1	1	2.28 · 10 ³
4	3.03	2.443	-131.3	673.4	207.1	1	466
5	5.27	6.773	-117.6	1927	162.2	1	98.9
6	18.2	13.299	-120.3	5390	87.01	1	43.7
7	16.5	27.497	-111.1	3945	95.81	1	73.9
8	18.7	31.016	-110.8	1671	89.98	1	467
9	19.6	32.510	-110.4	1001	87.89	1	1.36 · 10 ³
10	8.69	33.844	-111.1	688.2	132.2	1	1.28 · 10 ³
11	16.9	37.588	-114.8	4831	94.67	1	50.5
12	37.6	22.277	74.0	5037	65.45	1	103
13	15.8	25.115	76.6	1762	101.1	1	355
14	2.47	25.975	75.1	589.1	257.8	1	496

Table 3.2: Gaussian components for the observation of PKS 1451-375 obtained with the VLA. S_{8.6} displays the flux at 4.8 GHz, R and Θ are the polar coordinates with the core-component as the point of origin, a_{maj} is the major axis, a_{lim} the resolution limit of the major axis, Ratio the ration of the minor to the major axis, T_b the brightness temperature.

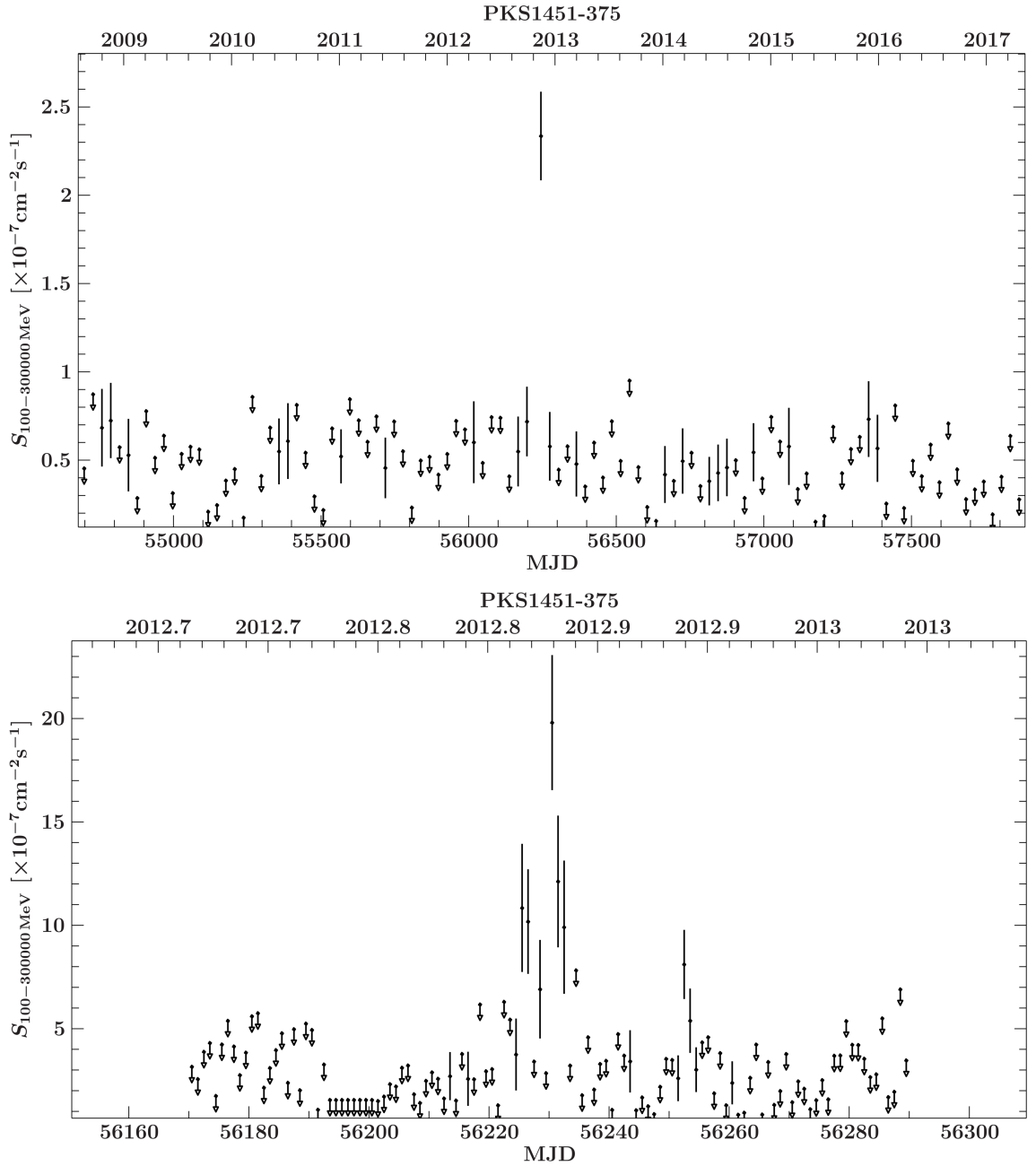


Figure 3.1: Fermi/LAT lightcurve of PKS 1451-375 in the energy range from 100 MeV to 300 GeV. Top: lightcurve with 30 days binning. The curve shows no prominent events with the exception of the flare in late 2012. Bottom: lightcurve with one-day binning. The rise and decrease of flux days around the flare in October 2010 are prominent. Also, a possible smaller second flare in November 2012 is visible. Credit: Michael Kreter (Universität Würzburg).

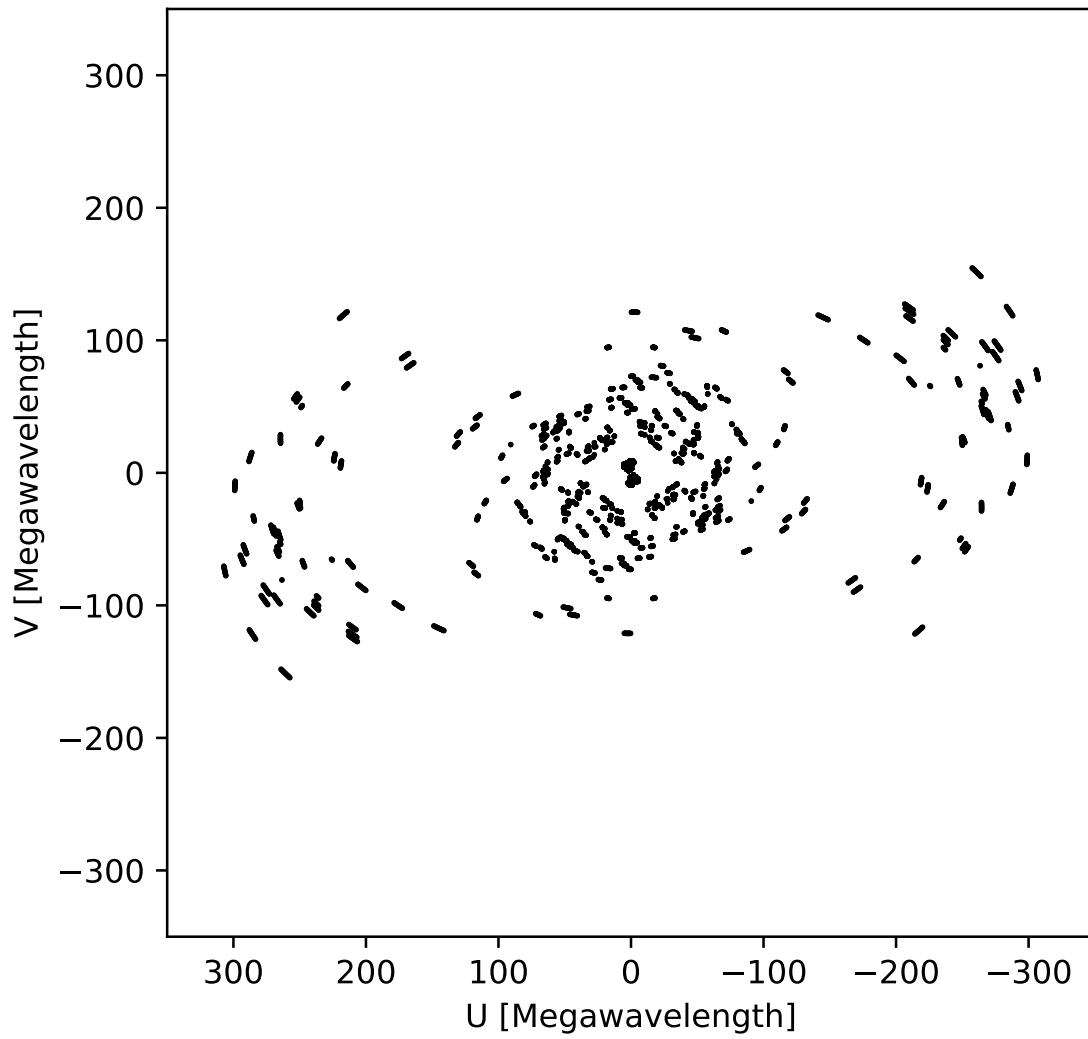


Figure 3.2: (u, v) -coverage for the observation of PKS 1451-375 with TANAMI.

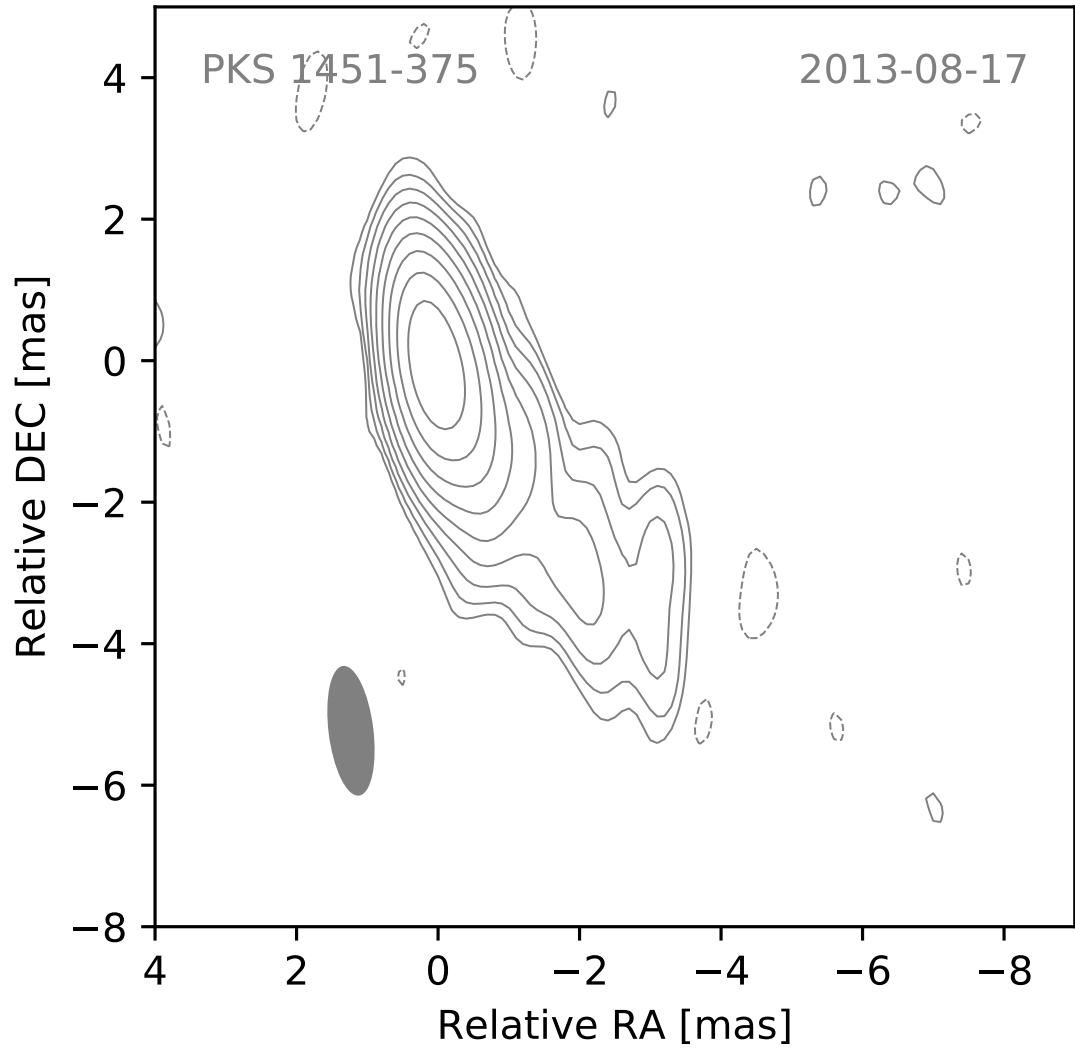


Figure 3.3: Clean map obtained with DIFMAP of PKS 1451-375 observed with TANAMI on August 17, 2013. Contour levels increase logarithmically while the smallest is set to the 3σ -noise level. The noise level is 0.60 mJy. The map peak is 0.853 Jy/beam. In the lower left corner the clean-beam is shown. The source shows a bright core and a jet in south-western direction.

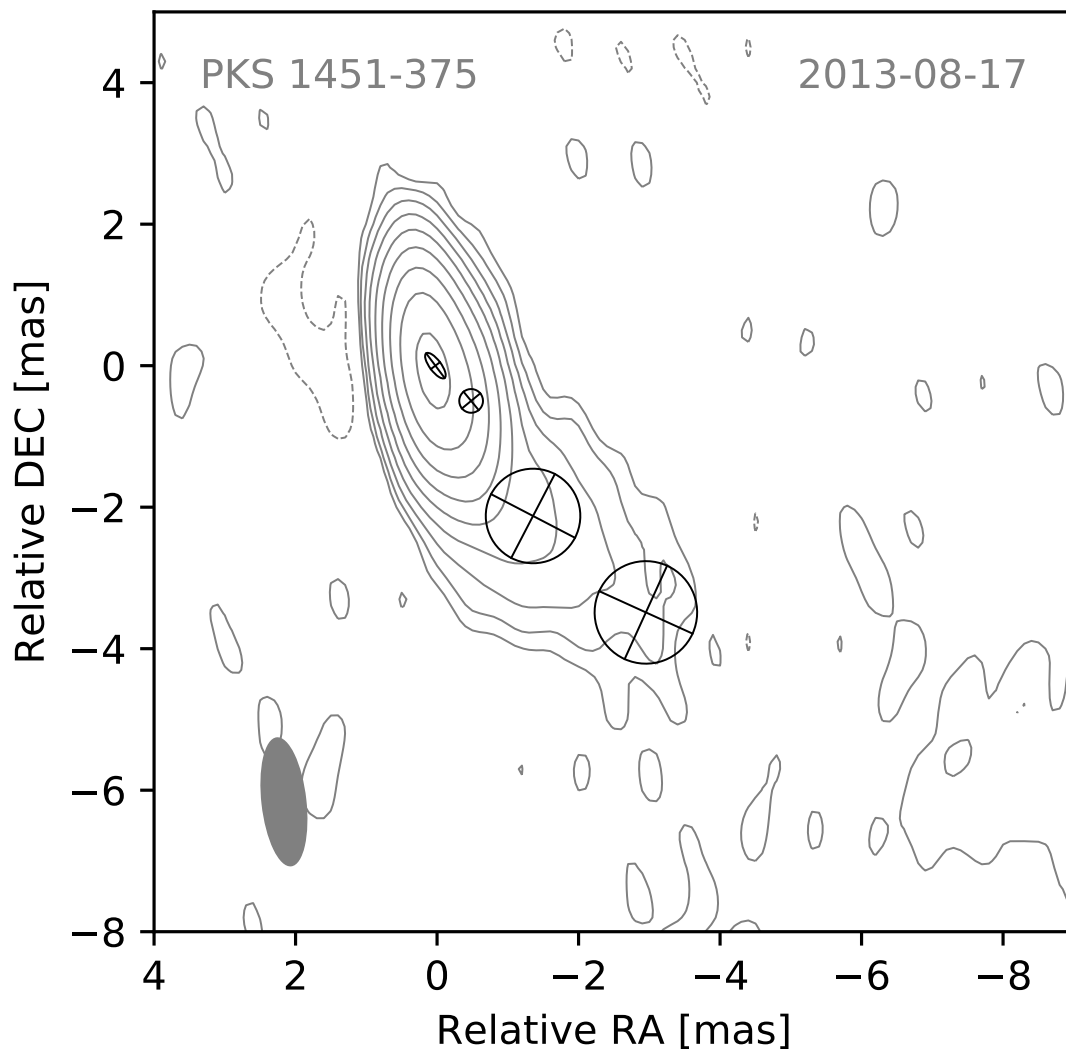


Figure 3.4: Map of PKS 1451-375 observed with TANAMI on August 17, 2013 plotted together with the Gaussian components obtained with `modelfit` in DIFMAP. The core component was allowed to be elliptical while the others had to remain spherical. Contour levels increase logarithmically while the smallest is set to the 3σ -noise level. The noise level is 0.88 mJy. The map peak is 0.836 Jy/beam.

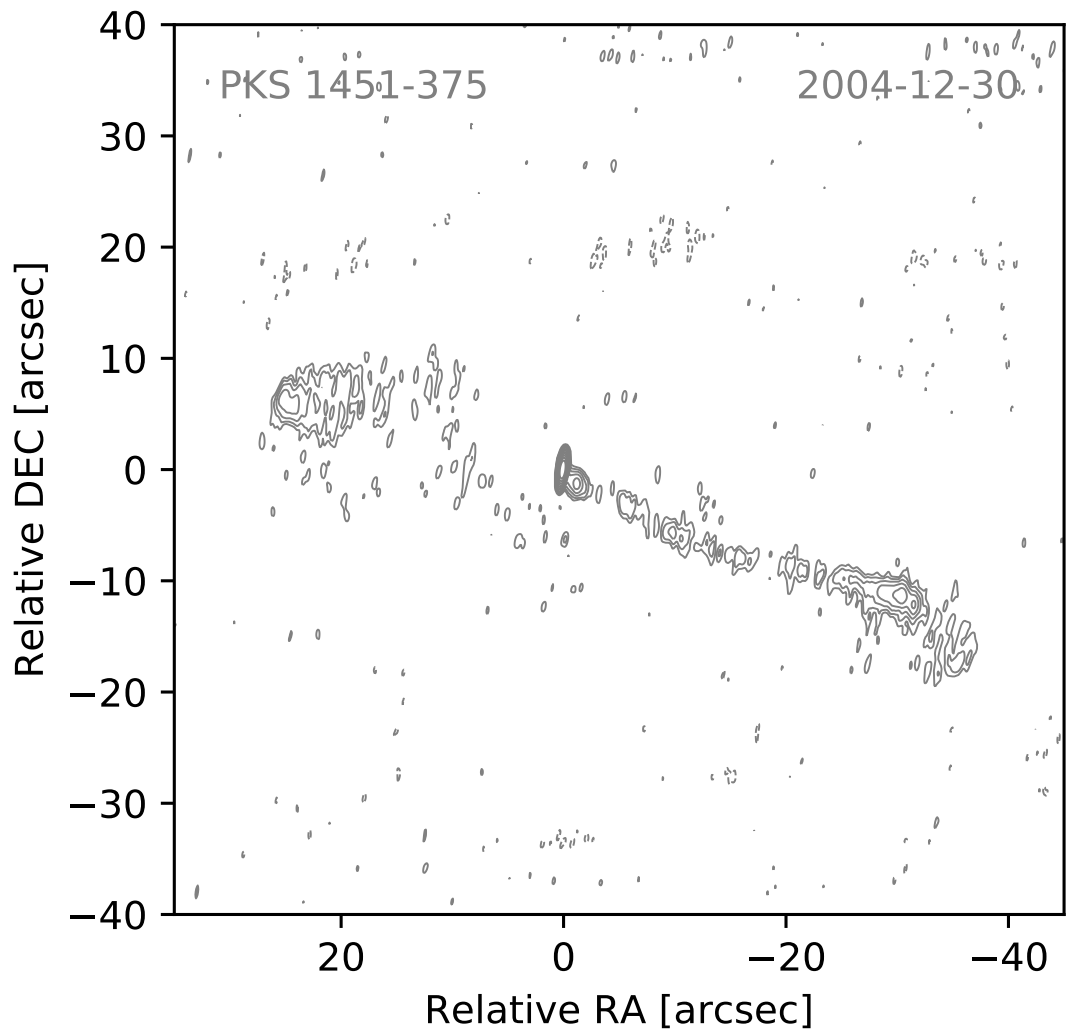


Figure 3.5: Clean map obtained with DIFMAP of PKS 1451-375 observed with the VLA on December 30, 2004. Contour levels increase logarithmically while the smallest is set to the 3σ -noise level. The noise level is 0.074 mJy. The map peak is 0.662 Jy/beam.

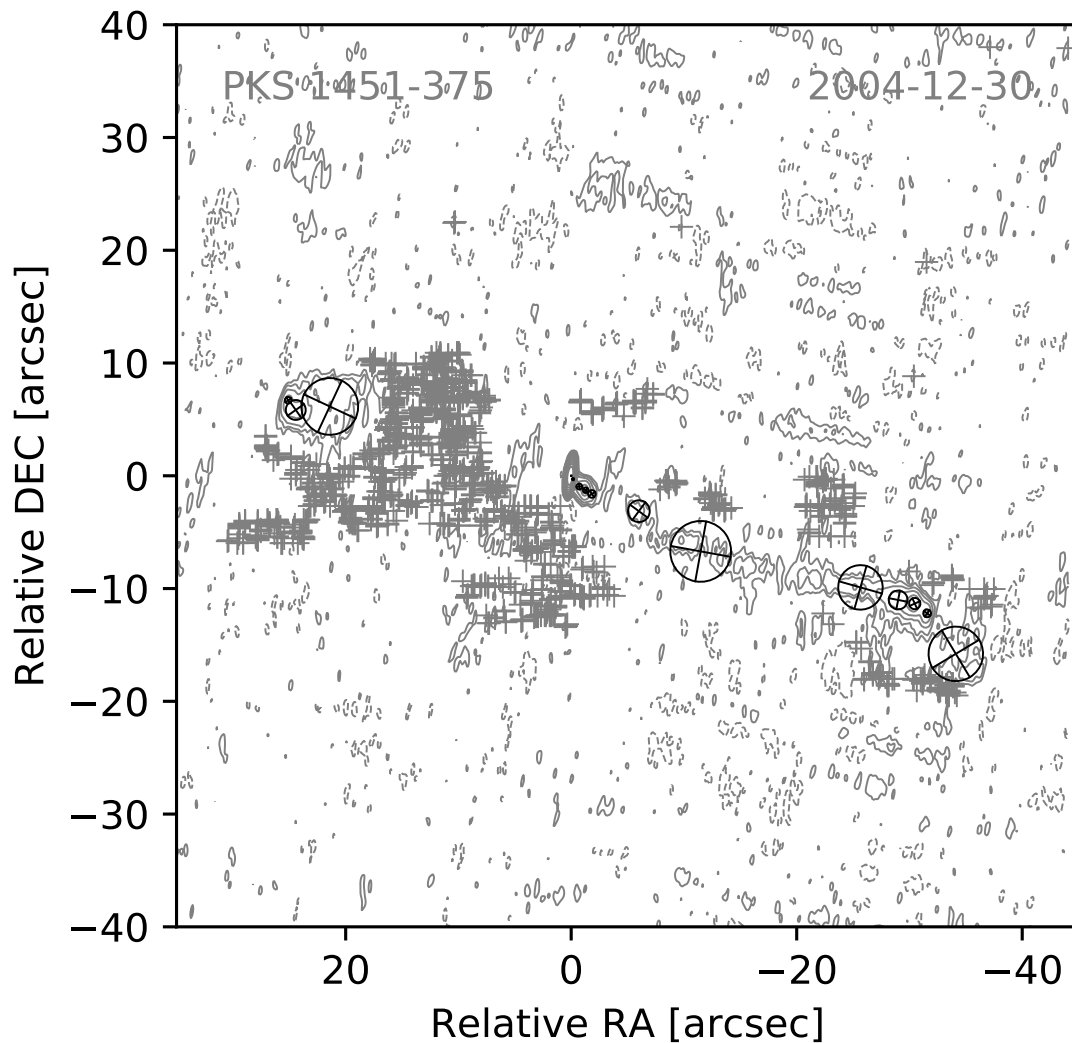


Figure 3.6: Map of PKS 1451-375 observed with the VLA on December 30, 2004 plotted together with the Gaussian components obtained with modelfit in DIFMAP. Only spherical components were allowed. Contour levels increase logarithmically while the smallest is set to the 3σ -noise level. The noise level is 0.074 mJy. The map peak is 0.853 Jy/beam.

4 Discussion

In this section, the results of the previous sections are used to determine some properties of the jet in both the TANAMI and the VLA observations. According to the work of Kadler et al. (2004), brightness temperature gradients are studied. Furthermore, a closer look at the two hotspots of the VLA observation is taken. PKS 1451-375 is compared to the previous observed AGN with TANAMI and a constraint of the inclination angle of the jet is done.

4.1 PKS 1451-375 in the TANAMI sample

In this section, PKS 1451-375 is put in context to the initial 43 sources in the TANAMI sample that are described by Ojha et al. (2010).

With a redshift of $z = 0.314$, PKS 1451-375 is in the low-redshift part of the sample. Only one quasar has a redshift below $z = 0.4$ but 13 galaxies and Bl Lac objects are below this limit. With PKS 1451-375 initially classified as a quasar but showing also a pronounced radio galaxy morphology in the VLA observation, it lies in the transition between those two classes. In the study of Ojha et al. (2010) 12 of the 43 sources were detected by Fermi/LAT, however only one of them is a galaxy.

With a core brightness temperature of $2.6 \cdot 10^{11}$ K, PKS 1451-375 lies above the mean value of $2.1 \cdot 10^{11}$ K but not very much and is, therefore, a very typical source, compared to the sample. However, as described in Sec. 1.1.3, this value is above the equipartition limit of 10^{11} K.

4.2 Jet Orientation

By calculating the jet-to-counterjet-ratio and making some justified assumptions, the angle to the line of sight of the jet for the TANAMI observation can be estimated. Solving Eq. 1.4 for ϕ leads to

$$\phi = \arccos \left(\frac{1}{\beta} \frac{R^{1/p} - 1}{R^{1/p} + 1} \right).$$

Since no counterjet is visible, only a lower limit for the jet-to-counterjet-ratio can be given by assuming the flux density of the counterjet to be smaller than the noise in this region. Defining the jet to be component 1, 2 and 3 with a total flux density of 385 mJy this leads to a lower limit for R of $R > 642$.

As multiple components are taken into account, $p = 2 + \alpha$. It is assumed that $\beta = 1$ which is reasonable for a highly relativistic jet and that $\alpha = 0$ which is justified by the previous spectral analysis (see Chapter 2.2). This leads to an upper limit for the inclination angle of

$$\phi < 22.5^\circ.$$

4.3 Hotspots

Although there is no full excepted definition of a hotspot, Bridle et al. (1994) defined it as the brightest feature in the radio lobes that are away from the core than any jet. It needs to be brighter by a factor of four than any extended diffuse emission. The two bright structures that are visible in the VLA observation match this definition and are referred to as hotspots from now on. To the hotspot south-west of the core, component 9 of the modelfit analysis is associated because it sits in the highest contour level and has also the highest brightness temperature in this region. The association of the hotspot north-east of the core is not that clear. The highest contour level is occupied by the components 13 and 14 and for further analysis, the mean value for the size and the distance to the core of those two components is handled as the hotspot. Table 4.1 shows both hotspots together with their major axis and the distance from the core.

Jeyakumar and Saikia (2000) analyzed the relationship between the sizes of hotspots and the overall size of high-luminosity FR 2 galaxies. Fig. 4.1 shows the hotspot size of these sources plotted against their overall size (LAS for largest angular size). A power-law describes the distribution with a power-law index of 1.02 ± 0.06 . The position of PKS 1451-375 in this plot is marked with a red point (without errors) where the hotspot size is the average of the two hotspots shown in table 4.1 and the largest angular size is sum of the distances of the hotspots to the core. The point lies in the distribution of the other sources and shows that this source is comparable to the sample of high-luminosity FR 2 galaxies.

Based on this distribution, Burd (2017) established a method for constraining the inclination angle of a source that is comparable to the sample of Jeyakumar and Saikia (2000). The inclination angle is according to Burd (2017)

$$\phi = \arcsin \left(\frac{\tan \left(\frac{\zeta}{2} \right)}{\tan \left(\frac{\zeta'}{2} \right)} \right) \quad (4.1)$$

with the apparent jet opening angle ζ' and the intrinsic jet opening angle ζ . The apparent jet opening angle can be calculated with

$$\zeta' = 2 \arctan \left(\frac{d}{2r} \right)$$

where d is the diameter of the hotspot and r the distance to the core. If ζ is unknown for a given source, ϕ can be estimated by comparing the jet to a large sample of sources with a well-known opening angle, in this case, the sample of Jeyakumar and Saikia (2000). Fig. 4.2 shows the distribution of the intrinsic jet opening angle for this sample of galaxies. The most probable opening angle is $\zeta_{mp} = 2.5^\circ$, the minimum $\zeta_{min} = 1.4^\circ$ and the maximum opening angle $\zeta_{max} = 19.6^\circ$.

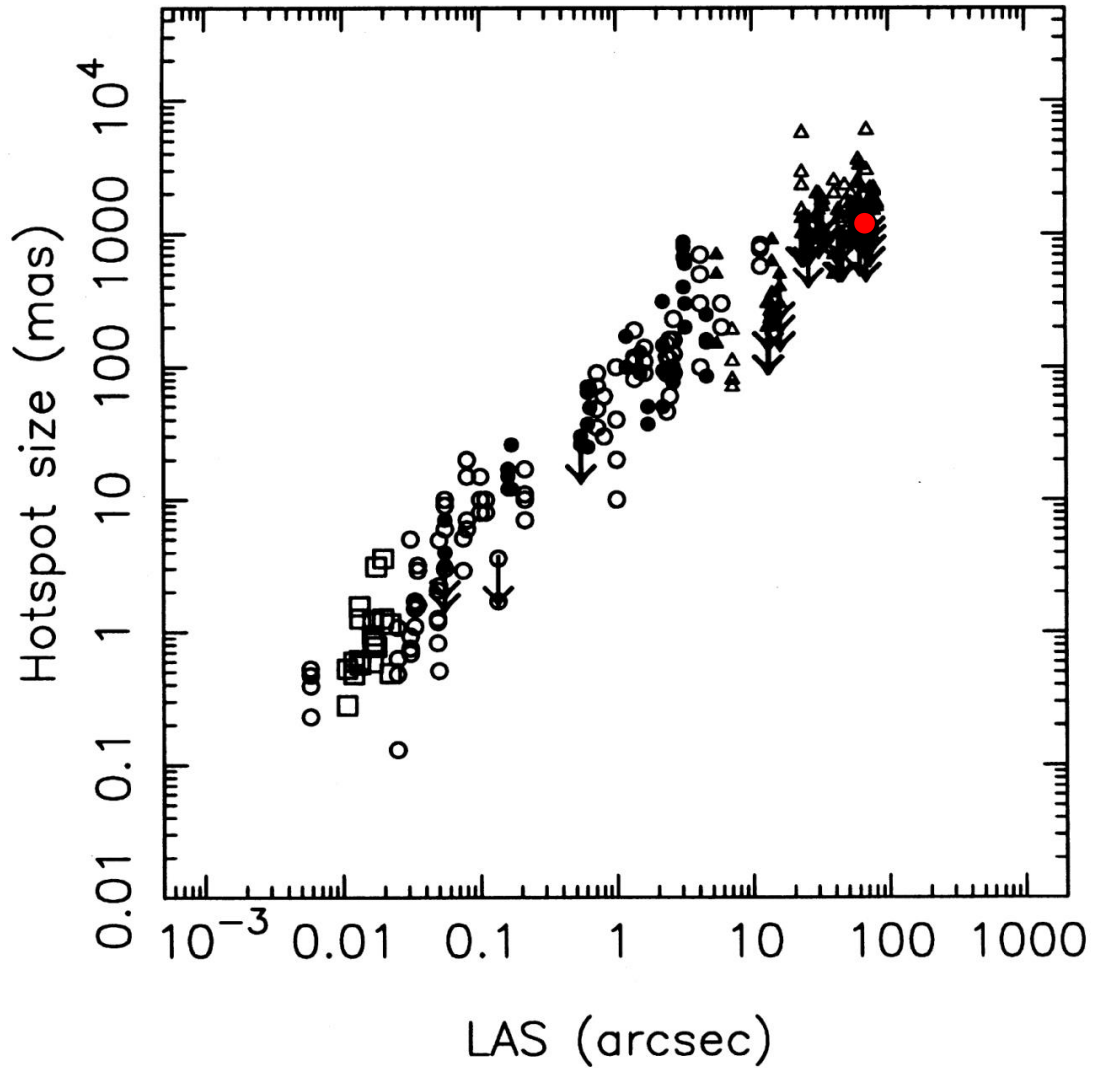


Figure 4.1: The hotspot size plotted against the largest angular size (LAS) of the source for a sample of high-luminosity FR 2 galaxies. A power-law describes the distribution with a power-law index of 1.02 ± 0.06 . The red point shows the position of PKS 1451-375 with the average of the two hotspots. From: Jeyakumar and Saikia (2000), edited by Luis Wachter.

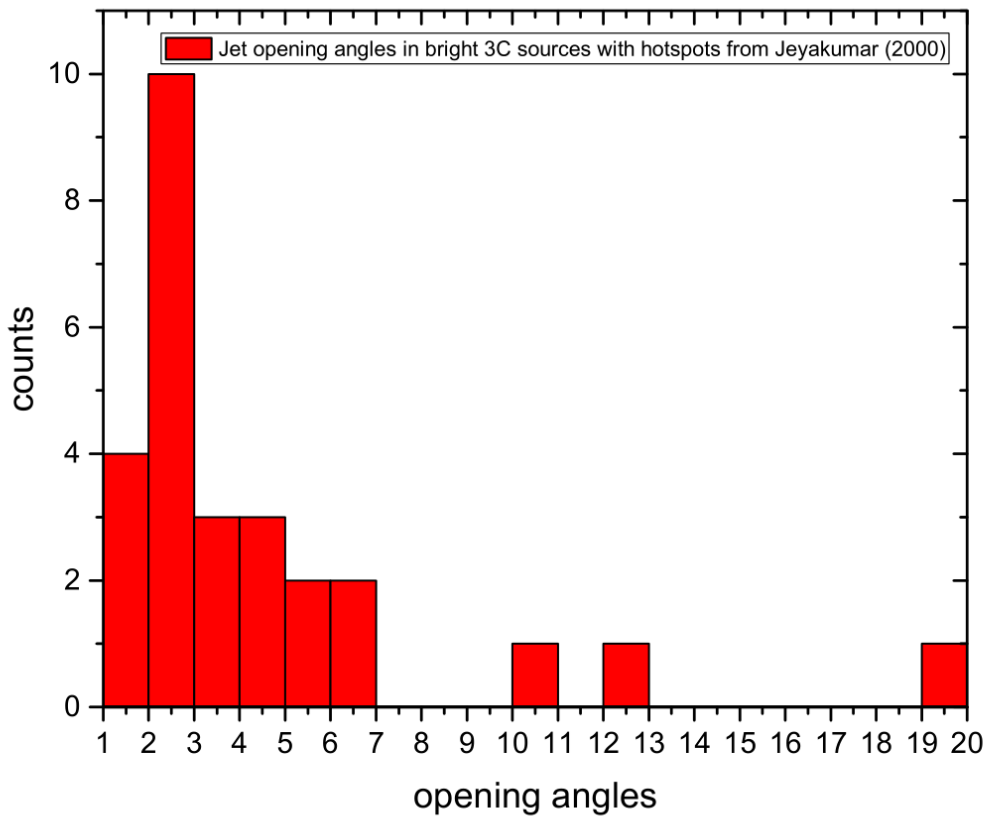


Figure 4.2: The distribution of the intrinsic jet opening angle in the sample of high-luminosity FR 2 galaxies from Jeyakumar and Saikia (2000) with 1° binning. From: Burd (2017).

With this distribution, a lower limit of the opening angle of an unknown jet can be estimated by calculating ϕ according to Eq. 4.1 with $\zeta = \zeta_{min}$.

For the hotspot south-west of the core this yields to a lower limit of

$$\phi_{SW} > 52.5^\circ$$

and for the hotspot north-east of the core to

$$\phi_{NE} > 32.1^\circ.$$

Hotspot	$S_{4.8}$ [mJy]	R [arcsec]	a_{maj} [mas]	apparent opening angle °
Component 9	19.6	32.510	1001	1.76
Mean of component 13 and 14	18.3	25.545	1176	2.64

Table 4.1: The two hotspots in the VLA observation. Component 9 is associated with the hotspot south-west of the nucleus and the mean values of Component 13 and 14 with the hotspot north-east. For the second hotspot the mean values for R and a_{maj} is given and the sum of the flux density of both components.

These values are not consistent with the upper limit of the inclination angle that is estimated before. However, as shown later, it is possible that the size of the hotspot is estimated to low and therefore the lower limit of ϕ to high for each hotspot. By assuming a conical jet and estimating the expected jet diameter at the distance of the hotspot south-west of the core with the power-law that is examined in the next section, the apparent jet opening angle would be $\zeta' = 17^\circ$ for both hotspots and therefore the lower limit of the inclination angle $\phi > 4.6^\circ$. Together with the upper limit from the previous section, the inclination angle can be therefore constrained to

$$4.6^\circ < \phi < 22.5^\circ$$

with the assumption that the hotspots do not exceed the power-law fit of the jet geometry.

At $\phi = 4.6^\circ$ PKS 1451-375 could still be called a blazar, however, an intermediate object between a Blazar and a radio galaxy is also plausible.

4.4 Brightness Temperatur Gradients

To study the jet geometry, the size of the Gaussian components of the jet is plotted against the distance to the core. Fig. 4.3 shows this plot. For the TANAMI observation, all components besides the core are shown. For the VLA observation, however, only the four components closest to the core are shown. Looking at Fig.

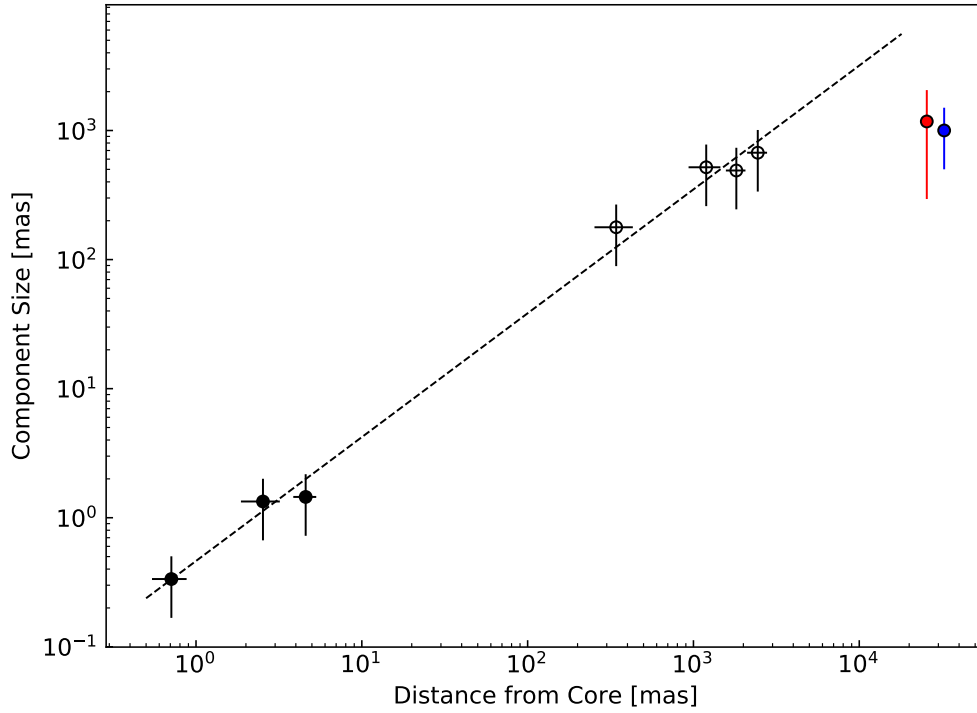


Figure 4.3: Plot of the major axis of a component against the distance from the core. TANAMI components are represented by filled circles and VLA components by open circles. For the TANAMI observations, all components excluding the core are plotted and for the VLA observation only the four closest to the core because they seem to represent the jet. Also plotted is the south-west hotspot of the VLA observation in blue and the mean values of the two components in the north-east that seem to represent the other hotspot in red. Because the jet appears to have the same geometry in both observations, only one power-law fit for both observations was made with a power-law index of $l = 0.960 \pm 0.033$. The hotspots were not taken into account.

3.6 one can see that only these components represent the continuous jet, while the following ones are only good to represent the left flux density.

Because no component is unresolved (see Chapter 3.2 for the resolution limit of a Gaussian component), the uncertainty for the distance as well as for the component size was estimated to 50% of the size of each component. The jet appears to maintain its geometry between the two different observation and therefore one power-law fit covering all components was made with a resulting power-law index of $l = 0.960 \pm 0.033$. This means that the jet is nearly conical (a perfect cone would have $l = 1$) and it matches nearly the canonical value of $l = 1$ given by Blandford and Königl (1979) and Konigl (1981).

Also plotted in Fig. 4.3 are the hotspots of the VLA observation. The blue data-point represents the hotspot in the south-west that belongs to the same jet than the other plotted components and the red data-point represents the mean value of the two components that are associated with the hotspot north-east of the core that however is not part of the same jet but the counterjet. They are not included in the fit and it is visible that they do not match with the power-law. However, one would expect that the jet retains the geometry until it interacts with the intergalactic medium at the hotspots. Therefore either a change in geometry takes place or the hotspot size is not represented by the chosen components. A further analysis with a tapered image could show if the size of the hotspots is not accurately estimated in this study.

Fig. 4.4 shows the brightness temperature gradient plotted against the distance from the core. The same components as in Fig. 4.3 are shown with the exception of the two hotspots. The uncertainty of the distance is again 50% of the components size. The uncertainty of the brightness temperature is composed of the error of the size and the flux density that is estimated to be 10%. However, the uncertainty is as big as the brightness temperature itself and therefore not presentable in the plot. Also, the data-points themselves indicate a different power-law for the two different observations and one could assume that the uncertainties are estimated too high. For better clearness errors of 50% for the brightness temperature are shown.

For each observation a power-law fit was made and the power-law indices according to Eq. 1.2 are $s_{TANAMI} = -3.46 \pm 0.14$ for the TANAMI observation and $s_{VLA} = -1.34 \pm 0.50$ for the VLA observation. s_{VLA} lies within its error in the range of the estimated value in tabel 1.2, s_{TANAMI} on the other hand exceeds the canonical value of s . The change in s between the two observations indicates that a change within the jet happens. Because the geometry and therefore l stays constant, either the magnetic field $B \propto r^b$, the particle density $n_e \propto r^n$, the spectral index α or a combination of those change their behavior between 4.585 mas and 342.4 mas.

This behavior is also visible in Fig. 4.5 where the brightness temperature is plotted against the size of each component. The uncertainties are the same as in Fig. 4.4 and the plot shows also that two different power-law fits are appropriate with the power-law indices according to Eq. 1.3 of $s_{l,TANAMI} = -3.8 \pm 1.2$ for the TANAMI observation and $s_{l,VLA} = -2.14 \pm 0.48$ for the VLA observation.

Because $s_d = s/l$ and $l = 1$, s_d is comparable to s in table 1.2 which is calculated

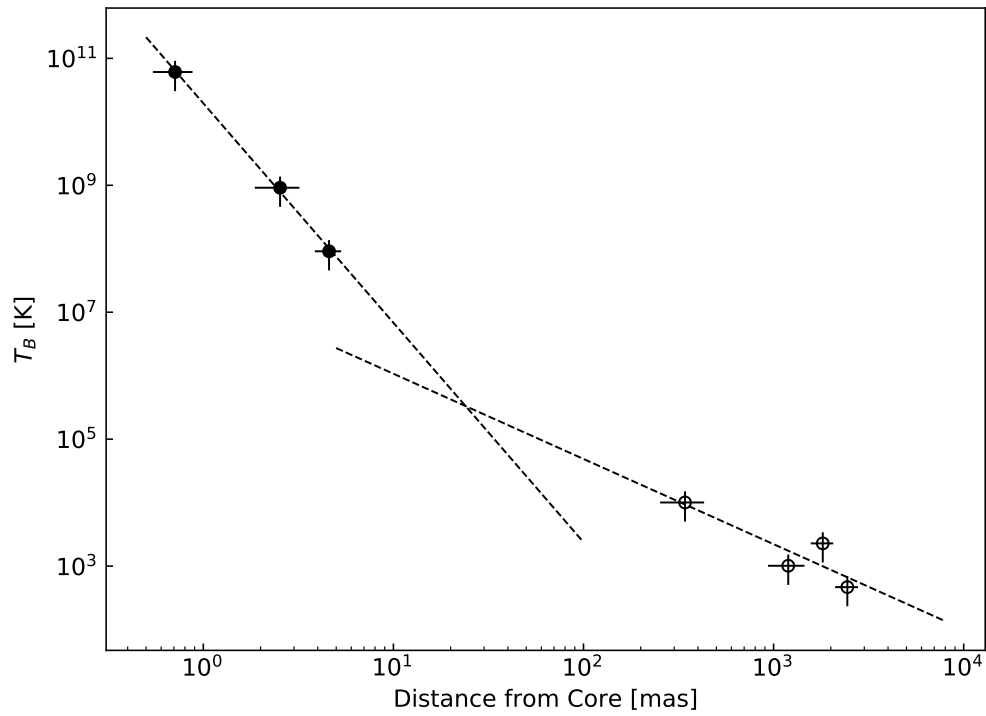


Figure 4.4: Brightness temperature gradient with T_b plotted against the distance from the core. TANAMI components are represented by filled circles and VLA components by open circles. A power-law fit was made for both observations with power-law indices of $s_{TANAMI} = -3.46 \pm 0.14$ for the TANAMI components and $s_{VLA} = -1.34 \pm 0.50$ for the VLA components.

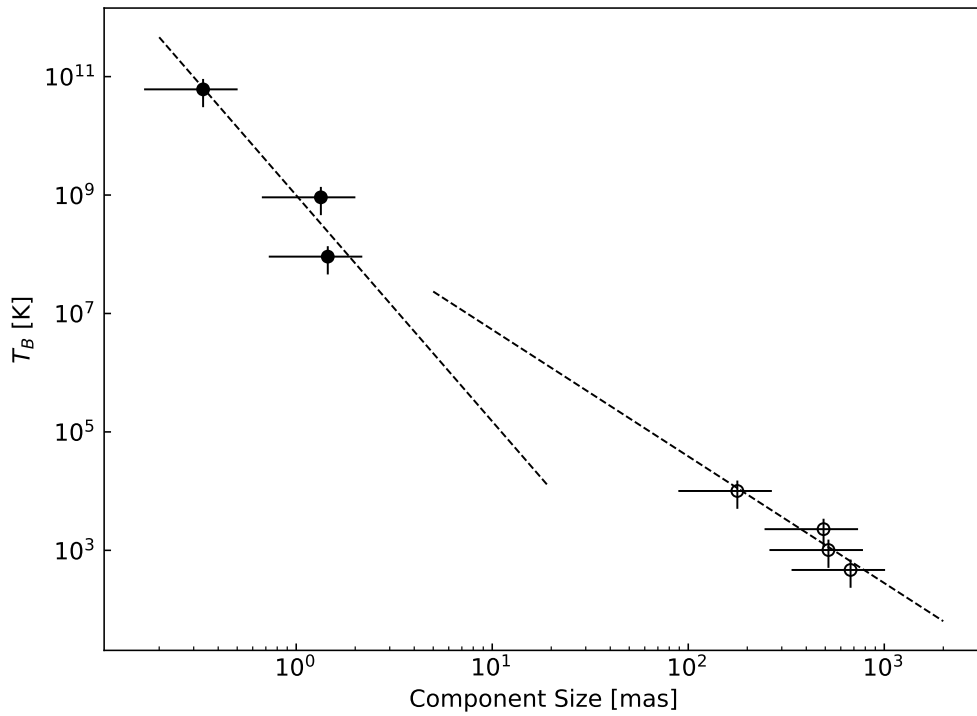


Figure 4.5: Brightness temperature gradient with T_b plotted against the major axis of the component. TANAMI components are represented by filled circles and VLA components by open circles. A power-law fit was made for both observations with power-law indices of $s_{l,TANAMI} = -3.8 \pm 1.2$ for the TANAMI components and $s_{l,VLA} = -2.14 \pm 0.48$ for the VLA components.

with the canonical values from Konigl (1981). Again, $s_{l,TANAMI}$ exceeds the canonical value and $s_{l,VLA}$ lies within the range.

Eq. 1.3 suggests that

$$l = \frac{s}{s_d} \quad (4.2)$$

and therefore for a conical jet with $l = 1$ one would expect that $s = s_l$. If l is calculated by Eq. 4.2 it will be referred as l_s and for the TANAMI and the VLA observation $l_{s,TANAMI} = 0.91 \pm 0.29$ and $l_{s,VLA} = 0.56 \pm 0.24$. $l_{s,TANAMI}$ match within its uncertainty with l from the power-law fit of the jet geometry and confirms the result of a nearly conical jet however $l_{s,VLA} = 0.56 \pm 0.24$ do not match. Table 4.2 shows all indices from the power-law fit, together with the calculated l_s according to Eq. 4.2.

	TANAMI	VLA
l	0.960 ± 0.033	0.960 ± 0.033
s	-3.46 ± 0.14	-1.34 ± 0.50
s_d	-3.8 ± 1.2	-2.14 ± 0.48
l_s	0.91 ± 0.29	0.56 ± 0.24

Table 4.2: The indices l , s and s_d for the power-law fits together with the calculated l_s .

5 Conclusion and Outlook

In this thesis, two observations of the AGN PKS 1451-375 were studied. The first observation made with TANAMI at 8.4 GHz showed a bright core with a jet of 5 mas in length in south-western direction. The second observation, made with the VLA at 4.8 GHz showed also a bright core and a jet in the same direction than the TANAMI observation. Additionally, two bright hotspots on opposite sides of the core are visible. This is the typical morphology of a FR 2 galaxy.

A modelfit analysis revealed that the jet is in both observations nearly conical and does not change its geometry. However, studying the gradient of the brightness temperature in regard to the distance to the core and the size of each component showed that a change in the jet happens between the two observations. This could either be a change in the magnetic field index, the particle density index or the spectral index. The modelfit analysis also showed a high brightness temperature of the core component in the TANAMI observation with $T_b = 2.1 \cdot 10^{11}$ K which is above the equipartition limit.

By calculating the jet-to-counterjet ratio an upper limit of $\phi < 22.5^\circ$ for the inclination angle was constrained. Another method of estimating the inclination angle is to compare the apparent jet opening angle of the source with a sample of FR 2 galaxies. This lead to a lower limit of $\phi_{SW} > 52.5^\circ$ and $\phi_{NE} > 32.1^\circ$ for both hotspots. Assuming the hotspots are estimated too small and the power-law of the jet geometry is still valid at the position of them, a lower limit of $\phi > 4.6^\circ$ for the inclination angle is given by the same method. Therefore, PKS 1451-375 could still be in the range of Blazars, however, an intermediate object between Blazars and radio galaxies is also plausible.

A tapered image would show if the size of the two hotspots are estimated too small in this study and if the jet geometry is conserved up to the hotspots. This would help to constrain the inclination angle more precisely. Studying a spectral index map and a polarization map could pinpoint the cause of change in the brightness temperature gradient because they would show changes in the two power-law indices for the magnetic field and the spectral index. Furthermore, with more very high-resolution observations with TANAMI, a kinematic analysis can show if the γ -flare in October 2012 lead to a new component in the jet.

References

- Antonucci, R. (1993). “Unified models for active galactic nuclei and quasars”. In: ARA&A 31, pp. 473–521. DOI: 10.1146/annurev.aa.31.090193.002353.
- Bastieri, D. (Nov. 2012). “Fermi LAT detection of a possible new gamma-ray FSRQ PKS 1451-375”. In: *The Astronomer’s Telegram* 4534.
- Beckmann, V. and C. R. Shrader (Aug. 2012). *Active Galactic Nuclei*.
- Blandford, R. D. and A. Königl (Aug. 1979). “Relativistic jets as compact radio sources”. In: ApJ 232, pp. 34–48. DOI: 10.1086/157262.
- Bridle, A. H. and R. A. Perley (1984). “Extragalactic Radio Jets”. In: ARA&A 22, pp. 319–358. DOI: 10.1146/annurev.aa.22.090184.001535.
- Bridle, A. H. et al. (Sept. 1994). “Deep VLA imaging of twelve extended 3CR quasars”. In: AJ 108, pp. 766–820. DOI: 10.1086/117112.
- Burd, P. R. (2017). “Long Wavelength Radio Observations of Blazars”. MA thesis. Julius-Maximilians-Universität Würzburg.
- Burke, Bernard F. and Francis Graham-Smith (2010). *An Introduction to Radio Astronomy* -. Cambridge: Cambridge University Press. ISBN: 978-0-521-87808-1.
- Chengalur, J. N. and N. Kanekar (Oct. 2000). “Implications of 21-cm observations for damped Ly α systems”. In: MNRAS 318, pp. 303–308. DOI: 10.1046/j.1365-8711.2000.03793.x. eprint: astro-ph/0011540.
- Fichtel, C. E. et al. (Oct. 1994). “The first energetic gamma-ray experiment telescope (EGRET) source catalog”. In: ApJS 94, pp. 551–581. DOI: 10.1086/192082.
- Fomalont, E. B. et al. (Nov. 2000). “The VSOP 5 GHz Continuum Survey: The Prelaunch VLBA Observations”. In: ApJS 131, pp. 95–183. DOI: 10.1086/317368.
- Greisen, E. W. (Mar. 2003). “AIPS, the VLA, and the VLBA”. In: *Information Handling in Astronomy - Historical Vistas*. Ed. by A. Heck. Vol. 285. Astrophysics and Space Science Library, p. 109. DOI: 10.1007/0-306-48080-8_7.
- Högbom, J. A. (June 1974). “Aperture Synthesis with a Non-Regular Distribution of Interferometer Baselines”. In: A&AS 15, p. 417.
- Jennison, R. C. (1958). “A phase sensitive interferometer technique for the measurement of the Fourier transforms of spatial brightness distributions of small angular extent”. In: MNRAS 118, p. 276. DOI: 10.1093/mnras/118.3.276.
- Jeyakumar, S. and D. J. Saikia (Jan. 2000). “Collimation of extragalactic radio jets in compact steep-spectrum and larger sources”. In: MNRAS 311, pp. 397–404. DOI: 10.1046/j.1365-8711.2000.03063.x. eprint: astro-ph/9904241.
- Johnston, K. J. et al. (Aug. 1995). “A Radio Reference Frame”. In: AJ 110, p. 880. DOI: 10.1086/117571.
- Kadler, M. et al. (Nov. 2004). “The twin-jet system in NGC 1052: VLBI-scrutiny of the obscuring torus”. In: A&A 426, pp. 481–493. DOI: 10.1051/0004-6361:20041051. eprint: astro-ph/0407283.
- Kadler, M. et al. (June 2015). “TANAMI: Multiwavelength and multimessenger observations of active galaxies”. In: *Astronomische Nachrichten* 336, p. 499. DOI: 10.1002/asna.201512186. arXiv: 1506.03947 [astro-ph.HE].

- Kellermann, K. I. and I. I. K. Pauliny-Toth (Feb. 1969). “The Spectra of Opaque Radio Sources”. In: ApJ 155, p. L71. DOI: 10.1086/180305.
- Kellermann, K. I. et al. (Oct. 1989). “VLA observations of objects in the Palomar Bright Quasar Survey”. In: AJ 98, pp. 1195–1207. DOI: 10.1086/115207.
- Konigl, A. (Feb. 1981). “Relativistic jets as X-ray and gamma-ray sources”. In: ApJ 243, pp. 700–709. DOI: 10.1086/158638.
- Kovalev, Y. Y. et al. (Dec. 2005). “Sub-Milliarcsecond Imaging of Quasars and Active Galactic Nuclei. IV. Fine-Scale Structure”. In: AJ 130, pp. 2473–2505. DOI: 10.1086/497430. eprint: astro-ph/0505536.
- Mannheim, K. (Mar. 1993). “The proton blazar”. In: A&A 269, pp. 67–76. eprint: astro-ph/9302006.
- Massardi, M. et al. (Feb. 2008). “The Australia Telescope 20-GHz (AT20G) Survey: the Bright Source Sample”. In: MNRAS 384, pp. 775–802. DOI: 10.1111/j.1365-2966.2007.12751.x. arXiv: 0709.3485.
- Müller, C. et al. (Sept. 2017). “TANAMI: Tracking Active Galactic Nuclei with Austral Milliarcsecond Interferometry - II. Additional Sources”. In: *ArXiv e-prints*. arXiv: 1709.03091 [astro-ph.HE].
- Ojha, R. et al. (Sept. 2010). “TANAMI: tracking active galactic nuclei with austral milliarcsecond interferometry . I. First-epoch 8.4 GHz images”. In: A&A 519, A45, A45. DOI: 10.1051/0004-6361/200912724. arXiv: 1005.4432.
- Pearson, T. J. and A. C. S. Readhead (1984). “Image Formation by Self-Calibration in Radio Astronomy”. In: ARA&A 22, pp. 97–130. DOI: 10.1146/annurev.aa.22.090184.000525.
- Perley, R. A. (Mar. 1981). “Radio jets in flat-spectrum sources”. In: *Optical Jets in Galaxies*. Ed. by B. Battrock and J. Mort. Vol. 162. ESA Special Publication.
- Perley, R. A. et al. (Oct. 1979). “The structure of the radio jets in 3C449”. In: Nature 281, pp. 437–442. DOI: 10.1038/281437a0.
- Perley, R. A. et al. (Sept. 2011). “The Expanded Very Large Array: A New Telescope for New Science”. In: ApJ 739, L1, p. L1. DOI: 10.1088/2041-8205/739/1/L1. arXiv: 1106.0532 [astro-ph.IM].
- Peterson, B. A. and J. G. Bolton (Jan. 1972a). “Identification of Southern Quasi-Stellar Objects-II”. In: Astrophys. Lett. 10, p. 105.
- (Apr. 1972b). “Redshifts of Southern Radio Sources”. In: ApJ 173, p. L19. DOI: 10.1086/180909.
- Pushkarev, A. B. and Y. Y. Kovalev (Aug. 2012). “Single-epoch VLBI imaging study of bright active galactic nuclei at 2 GHz and 8 GHz”. In: A&A 544, A34, A34. DOI: 10.1051/0004-6361/201219352. arXiv: 1205.5559.
- Quiniento, Z. M. and M. M. Echave (June 1990). “Radio spectra of quasars. II”. In: A&AS 83, pp. 393–398.
- Rybicki, G. B. and A. P. Lightman (1979). *Radiative processes in astrophysics*.
- Saikia, D. J. et al. (Aug. 1998). “Polarization observations of the radio cores of AGN - I. A sample of quasars”. In: MNRAS 298, pp. 877–887. DOI: 10.1046/j.1365-8711.1998.01699.x.

- Salpeter, E. E. (Aug. 1964). “Accretion of Interstellar Matter by Massive Objects.”
In: *ApJ* 140, pp. 796–800. DOI: 10.1086/147973.
- Shepherd, M. C. (1997). “Difmap: an Interactive Program for Synthesis Imaging”.
In: *Astronomical Data Analysis Software and Systems VI*. Ed. by G. Hunt and
H. Payne. Vol. 125. Astronomical Society of the Pacific Conference Series, p. 77.
- Thompson, A. R. et al. (Oct. 1980). “The Very Large Array”. In: *ApJS* 44, pp. 151–
167. DOI: 10.1086/190688.
- Urry, C. M. and P. Padovani (Sept. 1995). “Unified Schemes for Radio-Loud Active
Galactic Nuclei”. In: *PASP* 107, p. 803. DOI: 10.1086/133630. eprint: astro-
ph/9506063.

Acknowledgments

First and most of all I want to thank Matthias Kadler. He gave me the opportunity to do this project and supervised me during the work on it. His classes on extragalactic jets raised my interest in this topic and provided me with a broad basic knowledge of active galactic nuclei which helped a lot for this thesis.

I want to thank Jonas Ringholz for supporting me from the start of my work. He helped me by answering scientific questions, questions regarding DIFMAP and Python and also calibrated the VLA data.

I thank Paul Ray Burd for his support and helpful discussions. He introduced me to radio astronomy in the Astrophysical Laboratory Course and set, therefore, the basement for my thesis. With his Master thesis, he provided also the method of constraining the inclination angle.

I want to thank Michael Kreter, who provided the Fermi lightcurves and helped me regarding all Fermi questions.

Thanks to all members of the chair of astronomy who encouraged me and provided a friendly atmosphere during the time.

A special thanks to my family who made my studies possible and always supported my decisions. And to Antonia, who encouraged me during the whole time and who is always there for me.

This research has made use of the NASA/IPAC Extragalactic Database (NED) which is operated by the Jet Propulsion Laboratory, California Institute of Technology, under contract with the National Aeronautics and Space Administration.

This research has made use of the United States Naval Observatory (USNO) Radio Reference Frame Image Database (RRFID).

Declaration of authorship

I, Luis Wachter, hereby declare that I am the sole author of this thesis. I have not used any sources other than those listed and made it clear when I have consulted the work of others. This thesis was not submitted at any other institution before.

Place, Date

Signature